Applied Thermal Engineering 279 (2025) 127687

Contents lists available at ScienceDirect

Applied Thermal Engineering

journal homepage: www.elsevier.com/locate/apthermeng

Droplet impact on heated solid surfaces: from experimental and numerical approaches to dynamic behavior

Bin Li [a], Shiji Lin [b], Min Yang [c], Bingyang Cao [a,*]

[a] *Key Laboratory for Thermal Science and Power Engineering of Ministry of Education, Department of Engineering Mechanics, Tsinghua University, Beijing 100084, China*
[b] *Department of Mechanical and Aerospace Engineering, The Hong Kong University of Science and Technology, Clear Water Bay, Kowloon, Hong Kong*
[c] *National Key Laboratory of Spacecraft Thermal Control, Beijing Institute of Spacecraft System Engineering, Beijing 100094, China*

ARTICLE INFO

Keywords:
Droplet impact
Impact dynamics
Leidenfrost temperature
Spray cooling
Boiling regime

ABSTRACT

Collisional interactions between liquid droplets and elevated-temperature engineered surfaces now constitute a key technological challenge in advanced thermal management systems, particularly for high-flux cooling applications. The multiscale coupling of droplet-surface interactions spanning from molecular adhesion to hydrodynamic regimes governs the impact dynamics, where dynamic Leidenfrost transitions and nucleate boiling mechanisms establish thermal modulation as the predominant control parameter, and thus has been extensively investigated in recent years. An endeavor is made to provide an overview of the most recently developed experimental strategies for quantitative or qualitative determinations of droplet morphology evolution, internal flow, and the temperature fields during impact, in combination with the diverse simulation methods that enhance our understanding of these phenomena. This review summarizes various physical phenomena driven by the equilibrium of different forces, as well as the corresponding boiling regimes influenced by droplet and surface temperatures. Techniques for governing droplet rebound or Leidenfrost effect through surface modification and alterations in fluid properties, along with potential engineering applications are presented.

1. Introduction

The scientific exploration of droplet impact phenomena, spanning over a century of investigation, has been continually reinvigorated by its expanding technological relevance across multiple domains: from agricultural optimization through pesticide deposition [1], and infrastructure protection via raindrop erosion mitigation [2], to advanced manufacturing applications encompassing ink-jet printing [3], surface self-cleaning [4], and 3D printing [5]. Most recently, this field has gained renewed urgency from the thermal management challenges in high-power electronics [6], where droplet impact dynamics directly govern spray cooling efficiency for next-generation devices. Contemporary research primarily focuses on three thermal categories: subcooled, ambient, and superheated surfaces. Particularly, droplet impact dynamics on heated substrates has emerged as a pivotal research frontier, owing to its fundamental connection to spray cooling mechanisms [7] – an essential technology for next-generation thermal management systems requiring heat flux dissipation exceeding one hundred watts per square centimeter [8], far surpassing conventional air-cooling limitations [9–11].

This thermal management imperative stems from spray cooling's unique phase-change mechanism: when pressurized liquid undergoes atomization and subsequent droplet impingement on heated surfaces, it achieves unparalleled heat removal efficiency [12,13]. During the spray cooling process, the bubble nucleation density is notably higher than that in the traditional pool boiling [14]. This can be primarily ascribed to the fact that upon the arrival of the droplets at the free surface and their subsequent breakup, the free surface is substantially thinner compared to bulk liquids [15]. Moreover, in the case of spray cooling droplets, the bubbles do not detach from the heating surface due to buoyancy forces; instead, they remain continuously on the heating substrate. However, the inherent complexity of spray systems – characterized by interdependent parameters governing droplet dispersion [16] – necessitates fundamental investigations through isolated droplet experiments. Recent advances in ultrahigh-speed visualization [17–19] and nanoscale diagnostic techniques (e.g., total internal reflection microscopy [20]) have enabled unprecedented observations of transient impact phenomena, while numerical simulations [21–24] provide complementary insights into multiphase transport mechanisms.

---

* Corresponding author.
E-mail address: caoby@tsinghua.edu.cn (B. Cao).

https://doi.org/10.1016/j.applthermaleng.2025.127687
Received 25 April 2025; Received in revised form 23 July 2025; Accepted 26 July 2025

Nomenclature

Symbols

T	Temperature
u	Velocity
t	Time
P	Pressure
D_0	Initial diameter of droplet
R_0	Initial radius of droplet
D_i	Inner diameter of needle
D_o	Outer diameter of needle
H	Height of droplet's initial position
l_c	Capillary length
k	Thermal conductivity
F_g	Gravitational force
F_{st}	Surface tension force
F_{Lu}	Lubrication force
Q	Infusion rate
Q'	Heat source
V_0	Initial impact velocity
h	Thickness of vapor layer
T_w	Surface temperature
T_L	Leidenfrost temperature
T_{Tr}	Transition temperature
T_B	Boiling temperature
T_d	Droplet temperature
L	Latent heat

Dimensionless numbers

We	Weber number
Re	Reynolds number
Oh	Ohnesorge number
Bo	Bond number
St	Stokes number
Pe_ϕ	Péclet number
K	Splash number
Ca	Capillary number

Greek symbols

ρ	Density
σ	Surface tension
μ	Viscosity
g	Gravitational acceleration
τ_i	Dimensionless time
λ_{max}	Radiated peak wavelength
κ	Curvature of the interface
ζ	Timescale of Cahn–Hilliard diffusion
ω	Gas fraction
η	Dimensionless size of needle
β	Dimensionless spreading diameter
θ_{eq}	Contact angle
Θ	Volume fraction
ψ	Surfactant concentration
ϕ	Fluid interface

Key dimensionless parameters governing impact hydrodynamics include: Weber number ($We = \rho D_0 V_0^2/\sigma$): inertia-surface tension balance; Reynolds number ($Re = \rho D_0 V_0/\mu$): inertial-viscous forces ratio; Ohnesorge number ($Oh = \mu/(\rho\sigma D_0)^{0.5}$): the ratio of viscous forces to the combined effects of inertia and surface tension; Bond number ($Bo = D_0^2\rho g/\sigma$): gravity-surface tension interaction; capillary number ($Ca = \mu V_0/\sigma$): ratio of viscous forces to surface tension forces. These parameters dictate the energy conversion sequence: initial kinetic energy dissipation through radial spreading, followed by surface energy storage and viscous dissipation. Critical performance metrics include maximum spreading diameter [25–27] and contact time [28], both serving as essential indicators for mass-momentum-energy exchange efficiency. The spreading process is predominantly governed by the conversion between kinetic energy and viscous dissipation. The spreading diameter of a drop, which deforms upon impact with a solid surface, mainly depends on its Weber number (We) and Reynolds number (Re). Specifically, the larger the values of We and Re, the greater the value of β during the impact. During the receding phase, the retraction velocity of the droplet is governed by the balance between capillary pressure and fluid inertia. This equilibrium can give rise to an interconversion between deposition and rebound, and the contact time of the bouncing droplet is dictated by the capillary timescale. Recent breakthroughs demonstrate that these parameters can be systematically engineered through surface nano-structuring [29] and elastomeric substrate design [30]. The aforementioned dynamics will be elaborated in detail in the subsequent text.

The interplay between thermal gradients and hydrodynamic responses introduces multiscale complexity in droplet impact phenomena. An increase in surface temperature leads to a non-uniform temperature distribution across the droplet interface. This creates interfacial temperature gradients, which in turn generate surface tension gradients. manifesting as the Marangoni effect (fluid flow driven by such gradients along liquid interfaces). This effect induces convective Marangoni flows within the droplet. Consequently, the time required for a spreading droplet to attain its maximum diameter diminishes as the surface temperature rises. As the wall temperature rises, the impact dynamics undergo sequential phase transitions: initial contact-line deposition, followed by vapor nucleation and bubble encapsulation, ultimately evolving into partial or total rebound states [31]. Evaporation behaviors are categorized into four distinct regimes when stratified by thermal driving potential: non-boiling deposition, nucleate boiling with deposition, nucleate boiling – induced rebound, and vapor-film sustained Leidenfrost rebound [31,32]. Critically, the Marangoni effect plays a crucial role in modifying the force equilibrium during droplet evaporation [33], giving rise to self-thickening vapor-films and facilitating droplet rebound [34]. These intriguing regimes exhibit a remarkable sensitivity to three key governing parameters: nanoscale surface architecture [32], substrate heating conditions [35], liquid-phase physicochemical properties [36]. Crucially, nanoscale surface architecture plays a dominant role in determining surface wettability, which governs droplet impact behavior. Wettability is typically quantified by the contact angle—the angle at the solid–liquid-vapor contact line. While Young's equation prescribes a unique contact angle for an ideal flat surface, real manufacturing imperfections yield a range of observable angles bounded by advancing and receding values, a phenomenon termed contact angle hysteresis. Introducing micro/nano-scale roughness enables air pocket formation (Cassie state) or intrinsic hydrophobicity amplification (Wenzel state), facilitating superhydrophobic coatings via controlled nanostructures that minimize hysteresis and maximize repellency [37]. This nanostructure-driven control of wettability critically affects thermal phenomena, including the Leidenfrost point transition. Generally, enhanced wettability correlates with a higher Leidenfrost point [38], although exceptions arise depending on specific surface designs and conditions. Collectively, these phenomena and their underlying mechanisms establish droplet impact engineering as a multidisciplinary field bridging advanced surface design, non-equilibrium thermodynamics, and ultrahigh-heat-flux thermal regulation.

Furthermore, additional intricate factors give rise to complex impact outcomes. For instance, a depressurized environment [39] generates novel outcomes, such as magic carpet breakup and capillary rebound. Binary-mixture droplets [40] undergo a change in the boiling regime upon collision with a superheated surface. External forces, such as vibrations [41] or an electric field [42], modulate the Leidenfrost effect and impact outcomes. Although these phenomena fall outside the scope of this review, they are of great significance in engineering applications and exert a substantial influence on the dynamic behavior of droplets. In this review, a comprehensive overview of recent research methodologies and impact phenomena with potential applications related to the dynamics of droplet impact on heated solid surfaces is presented. A schematic framework outlining key research domains is depicted in Fig. 1. Finally, conclusions are reached, along with the identification of possible future research directions. These are intended to offer an in-depth understanding for controlling droplet impact, thereby inspiring further research in areas such as the performance assessment of engineering surfaces and the droplet impact dynamics in thermal engineering applications.

2. Experimental and numerical methods

2.1. Experimental platform

The experimental investigation of droplet collisional phenomena on heated surfaces typically incorporates the following key components (Fig. 2): a syringe pump to produce controlled droplets, a precision needle or capillary for liquid dispensing, a lifting table to adjust droplet release height, a high-speed camera to capture transient impact behavior, a controlled light source, a heating element to elevate the target surface temperature, and temperature sensors to monitor the system.

Previous investigations have predominantly focused on the dynamic interplay among interfacial tension, viscous dissipation and inertial contributions. To achieve gravitational decoupling in experimental protocols, droplets with characteristic dimensions below the capillary length [43] ($l_c = \sqrt{\sigma/\rho g}$) are preferentially selected. This dimensional constraint ensures Bond number suppression, as exemplified by standard experimental systems employing water ($l_c \approx 2.7$ mm) and ethanol ($l_c \approx 1.7$mm) droplets with initial radii $R_0 \lesssim 2$mm [44].

Liquid deposition studies predominantly employ monodisperse droplet configurations necessitating precise regulation of syringe pump discharge parameters. This precision engineering enables hydrodynamic

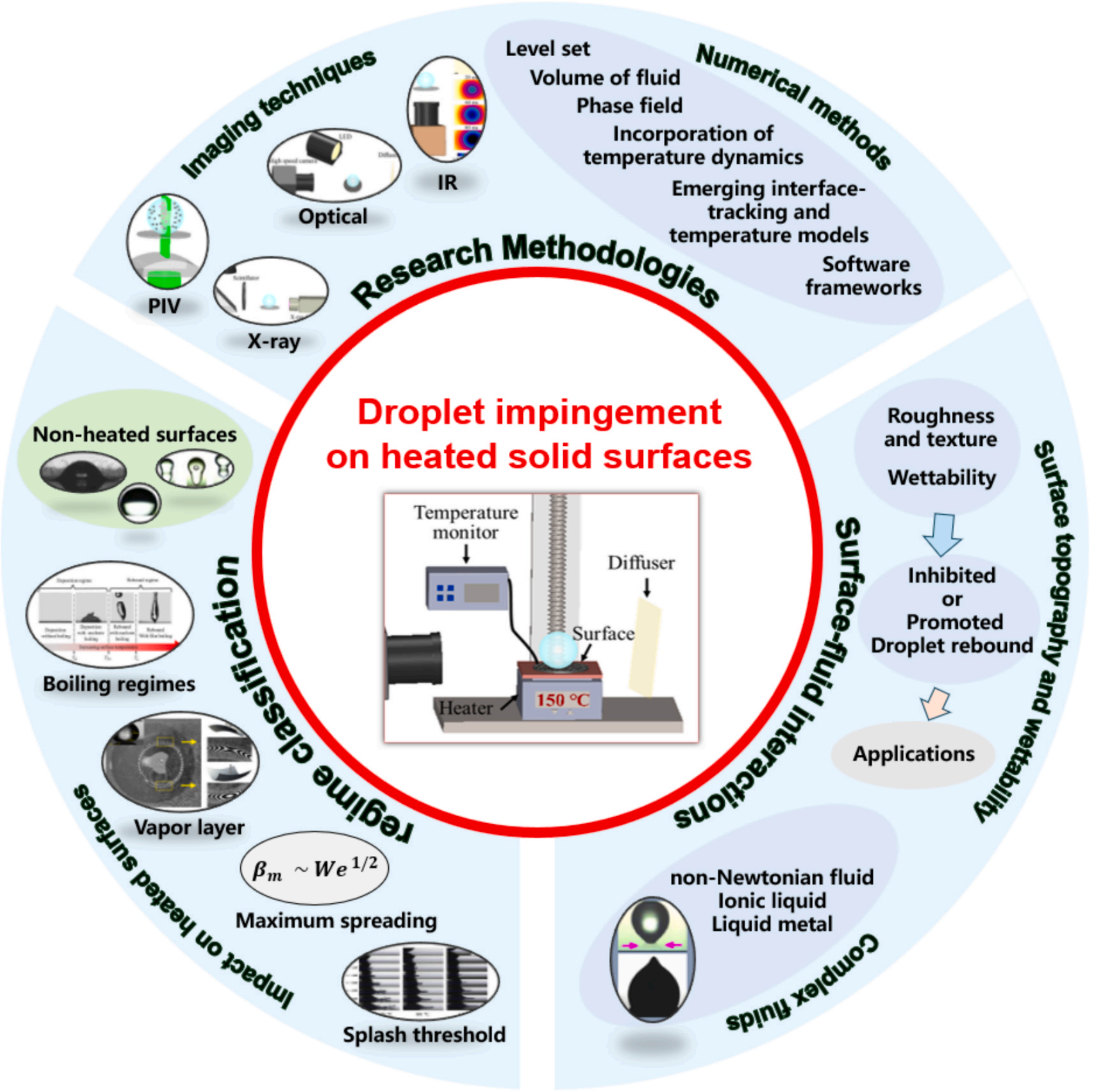

Fig. 1. Schematic framework delineating key research domains in this work.

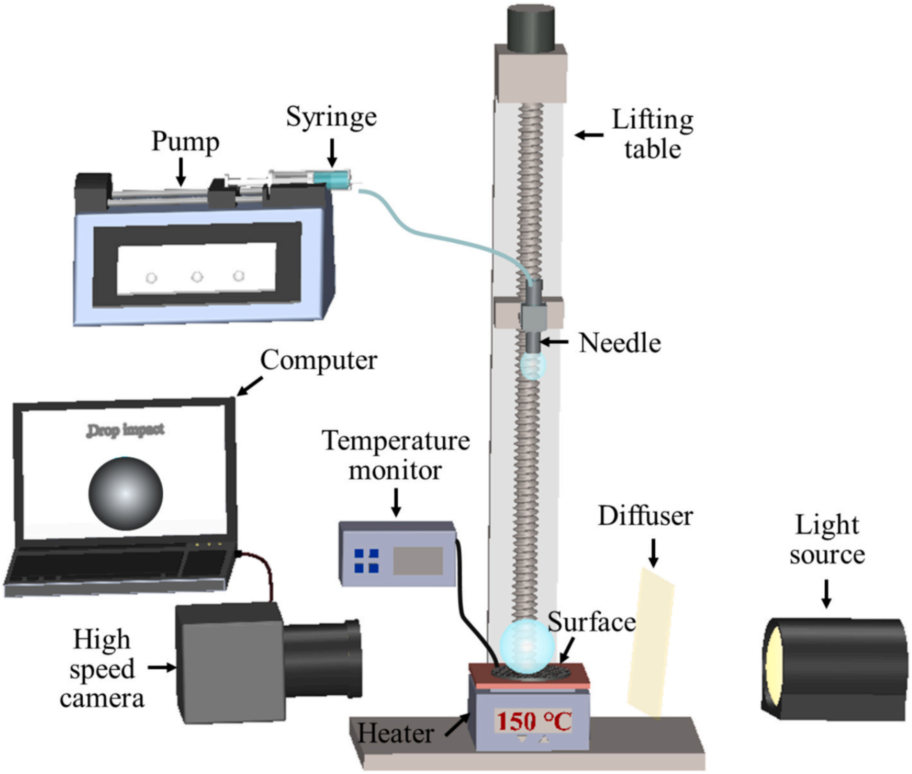

Fig. 2. Experimental platform for droplet collision on heated solid surfaces.

equilibrium during pendant droplet formation, where gravity triggers detachment upon surpassing capillary retention forces. A transition criterion from dripping to jetting behavior through dimensional analysis is derived [45]: $We_d = \rho V_j^2 D_i/\sigma = f(\rho, \gamma, g, D_i, D_o)$, with D_i and D_o the inner and outer diameters of the needle. Theoretical modeling predicts maximum sustainable discharge rates ($Q \approx 2000\mu\text{L/min}$ for $D_i = 60\ \mu\text{m}$ and $D_o = 240\ \mu\text{m}$ water dispensing systems) before jetting onset. Generally empirical protocols systematically implement subcritical flows ($Q = 100\ \mu\text{L/min}$) to maintain stable dripping kinematics [45].

Interfacial dynamics studies reveal distinct velocity modulation strategies across droplet scales. In millimetric regimes ($R_0 \approx 1\text{mm}$), gravitational potential modulation governs terminal velocity via free-fall height adjustment ($V_0 = \sqrt{2gH}$), as shown in Fig. 2. This quasi-static approximation holds when: (i) detachment dynamics satisfy $H \geq 10$ mm (neglecting initial momentum from capillary-driven formation processes) [46], and (ii) aerodynamic dissipation remains negligible during droplet fall, requiring direct measurement via high-speed videography [47]. To overcome hydrodynamic limitations, innovative momentum transfer architectures have been developed – centrifugal impaction systems achieve $V_0 = 50$ m/s ($We \approx 3 \times 10^5$) through substrate rotation [44]. In microfluidic domains ($R_0 = 10 - 100\ \mu\text{m}$), aerodynamic interactions dominate, leading gravitational acceleration impractical. Here, pulsed energy deposition techniques (electro-hydrodynamic actuation, laser-induced cavitation) enable ultrahigh-speed regimes ($V_0 = 100$ m/s) [48].

2.2. Imaging technique

2.2.1. Optical imaging

The high-resolution temporal tracking of interfacial topodynamics during droplet impingement events predominantly hinges on ultra-fast videometry [19,49], which is necessary to resolve topological transformations at the microsecond to millisecond scales. These Ultra-fast imaging modalities enable quantitative interrogation of interface evolution encompassing capillary-driven spreading/retraction cycles and free-surface wave propagation. This spatiotemporal coupling necessitates strict adherence to hydrodynamic similitude principles to clearly capture bulk transport phenomena.

For millimeter sized droplet, $10 - 100\,\mu\text{m}$ /pixel resolution is typically necessary [44,50,51], higher resolutions down to 1µm/pixel are required to observe microscale features like the bubble entrapment [52,53], singular jetting [54], and splashing [55]. The required temporal resolution is governed by the time scales implicated in the observed impact dynamics. During impact process, its relevant time scales of the overall impact process are scaled as $\tau_i \sim \left(\rho R_0^3/\gamma\right)^{1/2}$, ranging from 1µs to 1ms depending on the droplet radius. To adequately capture these fast-occurring phenomena, recording rates of 1000, 000fps may be necessary for 10µm droplets, while 1, 000 −10, 000fps suffices for millimeter-sized droplets [56,57].

High-intensity illumination (e.g., LEDs or lasers) is critical for such high-speed imaging. For clear visualization of the droplet morphology, shadowgraph imaging techniques with back lighting are often employed, as shown in Fig. 3(a). This method, however, sacrifices the ability to observe the internal flows within the droplet, as the parallel light rays primarily reflect off the droplet surface, leaving the interior relatively dark (Figs. 3(d) and 4(a)). To overcome this limitation, a diffuser-assisted illumination technique was utilized [58], as demonstrated in Fig. 3 (b–c). The enhanced visualization capability of diffused lighting is evident in Fig. 3 (e–f), where the expanded white light spots enable clear observation of internal structural developments within impacting droplets. This methodological advancement has been effectively employed in recent studies: cavity formation was successfully observed by utilizing back and side diffused illumination, as demonstrated in Fig. 4 (b-d) [58–60]. The backlighting configuration provides superior contrast imaging data, being particularly effective in quantifying morphological evolution and proving essential for the precise tracking of interfacial movement (Fig. 4 (b)). In comparison, the side diffused lighting can provide more detailed information about the internal flow structures and bubble dynamics within the impinging

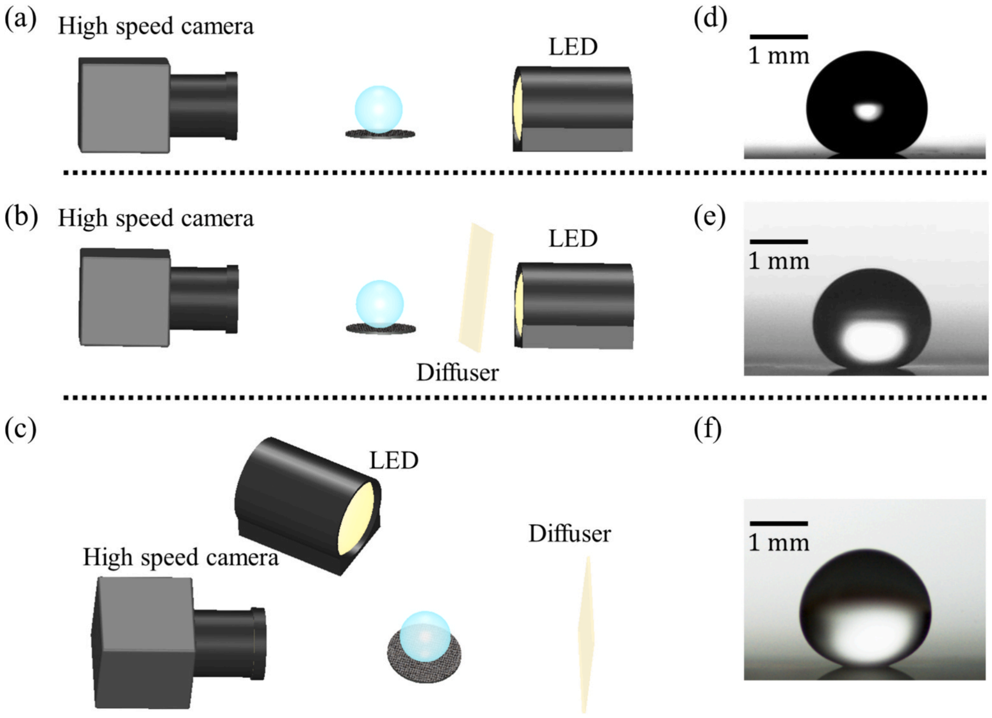

Fig. 3. Optical imaging using back and side lightings. (a) Back lighting without diffuser; (b) Back lighting with a diffuser. (c) Side lighting with a diffuser. (d-f) The resulting illuminations of droplets for the setups in (a-c), respectively.

droplet (Fig. 4 (c-d)).

The impact process may not be axisymmetric, such as splashing, and impact on inclined surfaces or inhomogeneous surfaces. In these scenarios, side-view imaging alone may be incomplete, requiring complementary bottom-view imaging to directly resolve interfacial phenomena between the droplet and surface. A typical experimental configuration involves positioning a 45° mirror beneath a transparent substrate, with a camera aligned to capture reflections from the mirror, as shown in Fig. 5 (a). Researchers have used this bottom-view imaging technique to study the impact on artificial surfaces, observing shock-like surface waves generated by microscale bumpy structures and the evolution of holes in the spreading droplet (Fig. 5 (b)) [62].

Through bottom-view imaging diagnostics, Maxim Piskunov et al. quantitatively characterized droplet fragmentation dynamics (Fig. 5 (c)), establishing a scaling law governing secondary droplet production through Weber-number-dependent fragmentation dynamics [63]. In parallel investigations, S.T. Thoroddsen et al. revealed extensive microbubble entrapment at liquid–solid interfaces during viscous droplet impacts on solid substrates (Fig. 5 (d)) [64].

Furthermore, the bottom-view imaging configuration enables quantitative characterization of thin gas films and microbubble entrapment through interferometric visualization. As illustrated in Fig. 5 (e), the experimental setup employs a precisely calibrated optical path where collimated laser illumination from the substrate side is split and focused onto the impact region through beam-steering optics. When approaching the substrate, the droplet generates dual reflective interfaces (solid-air and liquid–air) whose optical interference produces characteristic fringe patterns. The spatial frequency of these interference fringes exhibits an direct relationship with the air gap thickness [53,66]. Notably, Li and Thoroddsen pioneered the application of ultrahigh-speed interferometry with 200-ns temporal resolution to quantitatively track air film evolution throughout bubble entrapment processes, as demonstrated in Fig. 5 (f) [53]. Recent methodological advancements have further extended this interferometric approach to probe complex fluid phenomena, including the spatiotemporal evolution of levitated liquid films along lamella peripheries (Fig. 5 (g)) [65,67].

2.2.2. X-ray imaging

Complementing conventional visible-light optical techniques, X-ray imaging emerges as a powerful diagnostic tool for resolving internal dynamics in multiphase fluid systems. This methodology exploits the penetration and absorption of high-energy X-ray photons (0.1nm wavelength), which have a strong penetration capacity and low refractivity through materials, thereby enabling non-invasive tomography of embedded interfaces and subsurface features within impacting droplets [68]. Fig. 6 (a) schematically illustrates the essential components of a synchrotron-based X-ray imaging system. The experimental configuration comprises: (1) an X-ray source generating precisely timed photon bursts, (2) a high-efficiency detector assembly incorporating a fast-decay scintillator crystal for X-ray-to-visible-light conversion, coupled with (3) a 45° dichroic mirror directing the optical signal to a synchronized high-speed camera (CMOS/CCD) via precision opto-mechanical stages [69–71].

The breakthrough experimental campaigns conducted at Argonne National Laboratory's Advanced Photon Source have established new benchmarks in interfacial dynamics characterization, achieving simultaneous micron-scale spatial and microsecond temporal resolutions through synchrotron-based imaging [72,73]. A seminal investigation by Lee et al. employed phase-contrast radiography to resolve the complete morphological transition from entrapped air film to microbubble during droplet impact (Fig. 6 (b)) [72]. Their quantitative analysis revealed three distinct evolutionary phases: inertial-dominated film retraction, (ii) axisymmetric contraction culminating in bubble generation, and (iii) secondary droplet pinch-off, a tripartite mechanism initially hypothesized by Thoroddsen's group [74]. Recently, this X-ray phase-contrast imaging technology has been employed to monitor the growth of microbubbles on superhydrophilic textured substrates. This application enables an estimation of the heat transfer rate during droplet impact within the order of milliseconds [75]. The unique penetrative capacity of hard X-rays has further enabled groundbreaking observations in impact-induced splashing phenomena. High-flux X-ray tomography directly visualized the formation of toroidal vortex structures resulting from capillary-wave-mediated energy transfer during early impact

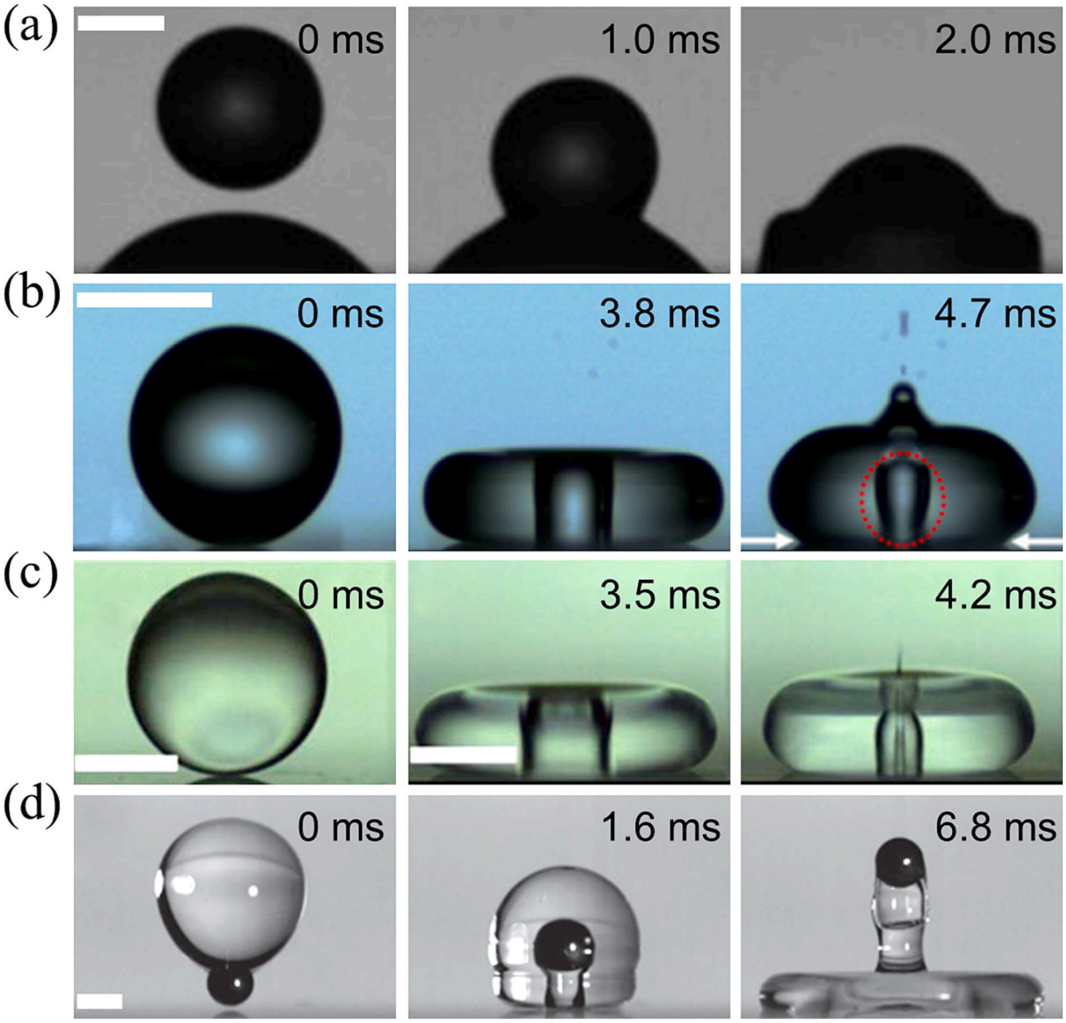

Fig. 4. Visualization of impinging droplet using different lighting methods. (a) Visualization of back lighting without a diffuser [61]; (b) Visualizations of back lighting with a diffuser [59]; (c) and (d) Visualizations using side lighting with a diffuser [58,60].

stages [71]. Expanding its investigative scope, this technique has decoded the hydrodynamic singularity formation mechanisms in liquid jetting events [76,77]. These paradigm-shifting results demonstrate that ultrafast X-ray imaging provides critical insights into previously inaccessible hydrodynamic singularities – from boundary layer separation to cavity collapse dynamics – that fundamentally challenge the resolution limits of visible-light diagnostics.

2.2.3. *Particle image velocimetry method*

While the above imaging techniques provide valuable insights into the external morphology and some internal phenomena during drop impact, they may fall short in capturing the detailed internal flow dynamics. Particle Image Velocimetry (PIV) addresses this limitation by providing quantitative, time-resolved velocity field measurements [78–81]. In a typical PIV setup, the fluid is seeded with fluorescent tracer particles (e.g. hollow glass spheres [82]). These particles should be small enough to accurately follow the fluid motion, yet large enough to provide sufficient light scattering for reliable detection. For the former condition, the Stokes number ($St = \rho_p d_p^2 V_0 / 18 D_0 \mu$) is calculated as the ratio of the particle relaxation time to the characteristic time scale of the fluid flow, where ρ_p and d_p are the particle density and diameter. A Stokes number much less than 1 ($St \ll 1$) indicates that the particles faithfully follow the fluid motion, which is the desired regime for accurate PIV measurements [83]. Regarding the imaging quality, the ideal size of the particle images is usually considered to be at least 3 pixels on the image sensor [84]. The resultant particle sizes are commonly in the range of $5 - 20\mu$m in diameter for drop impact experiment [81,85,86]. The tracer particles are illuminated using a laser sheet, and the emitted light from these particles is captured using high-speed imaging, as shown in Fig. 7 (a) and (c). Image processing techniques are applied to track the particle displacement between frames. PIV method can provide detailed velocity field measurements, enabling the study of fluid dynamics such as vorticity, shear rates, and flow structures during and after droplet impact.

Smith and Bertola employed PIV and found that impact the droplet spreads rapidly with the velocity increasing as a function of radius and decreasing as a function of time [80], validating previous analytical models to predict the velocity distribution [88–90]. Erkan and Okamoto resolved early-stage radial velocity profiles for low-Weber number impacts ($We \lesssim 15$), revealing a transition from linear to nonlinear behavior driven by upward flow instabilities (Fig. 7 (b)) [87,91]. Gultekin et al. extended this PIV-based investigation to higher Weber numbers (up to $We \approx 190$) and further validating theoretical frameworks for velocity distribution [78,88]. Complementing these studies, Rijn et al. used PIV to investigate the upward jets following drop impact (Fig. 7 (d)). Their work demonstrated that fluid elements within these jets could decelerate by $5 - 20$ times the gravitational acceleration, thereby providing the first quantitative explanation of the shape and dynamics of the jets [86]. Beyond the spreading and jetting dynamics, other impact phenomena, such as the evolution of ejecta sheets during splash, have also been

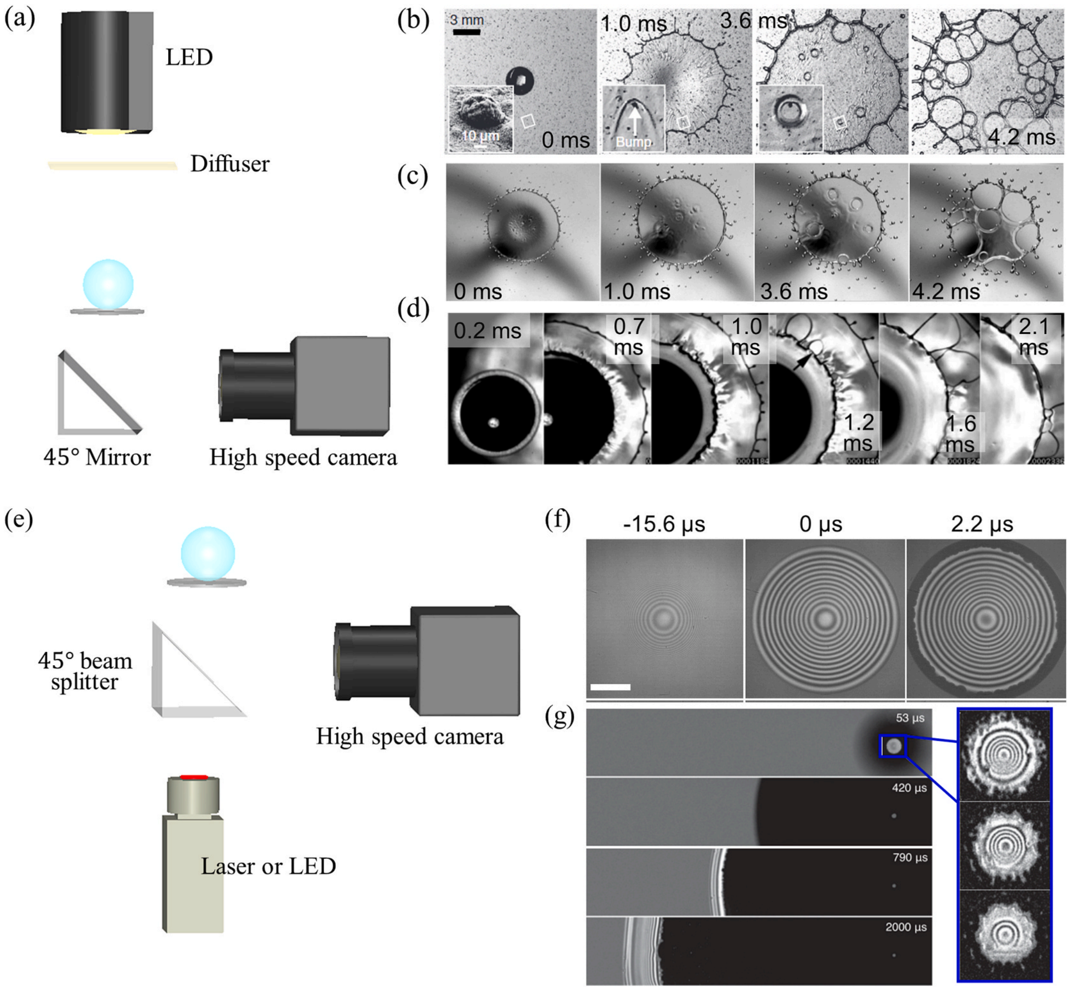

Fig. 5. Visualization of impinging droplet from the bottom view with lighting from top (a-d) and bottom (e-g). (a) Schematic of bottom view with lighting from top; (b) Shock-like surface waves and holes generated from the impact on artificial surfaces [62]; (c) Droplet breaking process after impact [63]; (d) Entrapment of microbubbles [64]. (e) Schematic of bottom view with lighting from bottom; (f) Interference fringes of central bubble [53]; (g) Interference fringes of both central bubble and levitated liquid film [65].

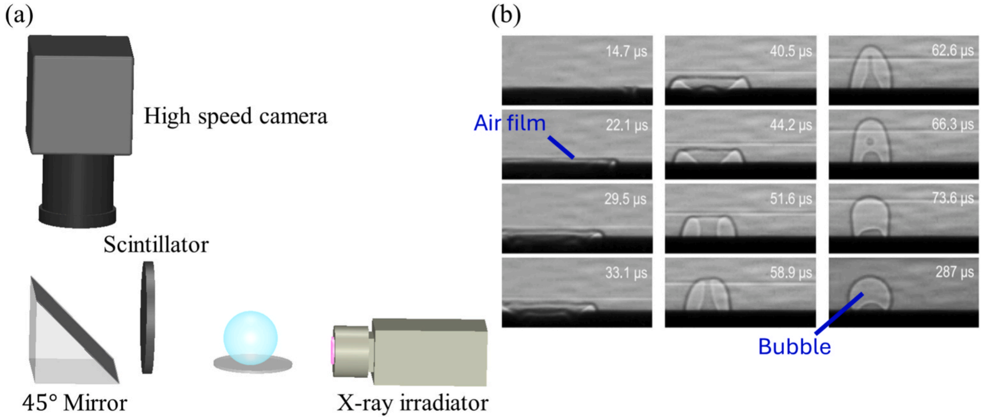

Fig. 6. Schematic of X-ray visualization of the impinging droplet (a) and (b) air film generation sequences during the impingement [72].

investigated using PIV techniques [92,93]. Most recently, researchers have begun to employ three-dimensional (3D) PIV approaches to capture the full spatiotemporal flow fields [94,95]. These advanced PIV methodologies offer the potential to provide unprecedented insights into the three-dimensional nature of the transient fluid dynamics and may see increased applications in future droplet impact studies.

2.2.4. *Infrared camera imaging*

Infrared (IR) camera imaging is a powerful tool for studying drop impact processes, particularly in thermal and material science applications. Initial experiments utilized thermocouple in point measurements of temperature [96–98], but IR imaging offers the ability to capture the full-field thermal response with high spatial and temporal resolution,

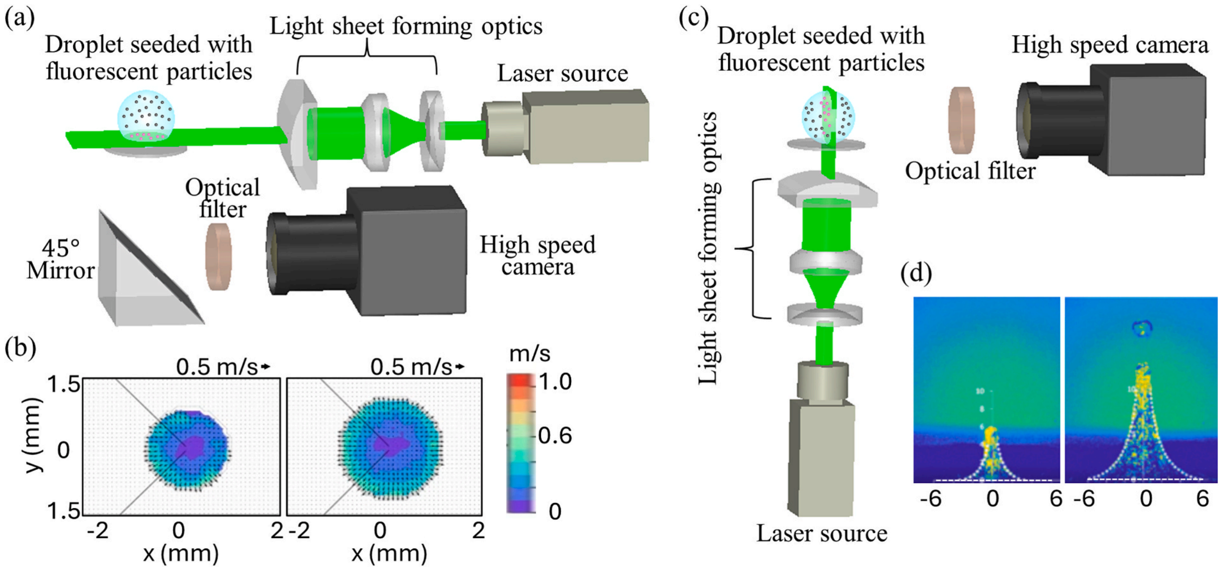

Fig. 7. Visualization of impinging droplet using PIV method. (a) Schematic of PIV method from bottom view; (b) Velocity vector fields obtained from the method described in (a) [87]; (c) Schematic of PIV method from side view; (d) Images taken using the method described in (c) [86].

providing valuable information on heat transfer, phase changes, and temperature distribution during impact process [98–101].

The imaging setup of IR camera is similar to that of optical high-speed camera, as shown in Fig. 8 (a) and (c). Unlike visible light imaging, IR cameras detect radiation from observing objects in the infrared spectrum [102]. According to the Stefan–Boltzmann law, the radiant emittance of an objects is proportional to the fourth power of the absolute temperature [103]. Additionally, Wien's displacement law states that the radiated peak wavelength λ_{max} is inversely proportional to the temperature T, i.e., $\lambda_{max} = b/T$, where $b = 2.898 \times 10^{-3}\mathrm{m} \bullet \mathrm{K}$ is the Wien's displacement constant [104]. For effective IR imaging, the IR camera's wavelength spectrum must align with the peak emission wavelength of the observed objects. Further, the IR camera must be calibrated for the expected temperature range [102]. Furthermore, the surface properties of the substrate, such as emissivity, must be well-characterized to ensure accurate temperature measurements [102]. Up to date, the best spatial and temporal resolutions of IR camera are in the range of 10 –100μm and 1 –10ms, respectively. Therefore, researchers commonly correlate thermal imaging with optical high-speed imaging.

Side-view has been widely adopted to identify the temperature distribution of the droplet upon impact [98,100] (Fig. 8(a)). To ensure the temperature monitored by the IR camera represents the drop surface temperature, the droplet material must be sufficiently opaque within the spectral range of the IR imaging system. For pure water droplets, it is nearly opaque in the mid-infrared wavelength range of approximately 3 –8 μm [105]. Liu et al. applied the IR imaging to reveal the transient thermal phenomena within a droplet impacting on heated surfaces, as demonstrated in Fig. 8(b) [98].

A bottom-view IR imaging is also popular to measure the transient temperature distribution at the interface between the droplet and the

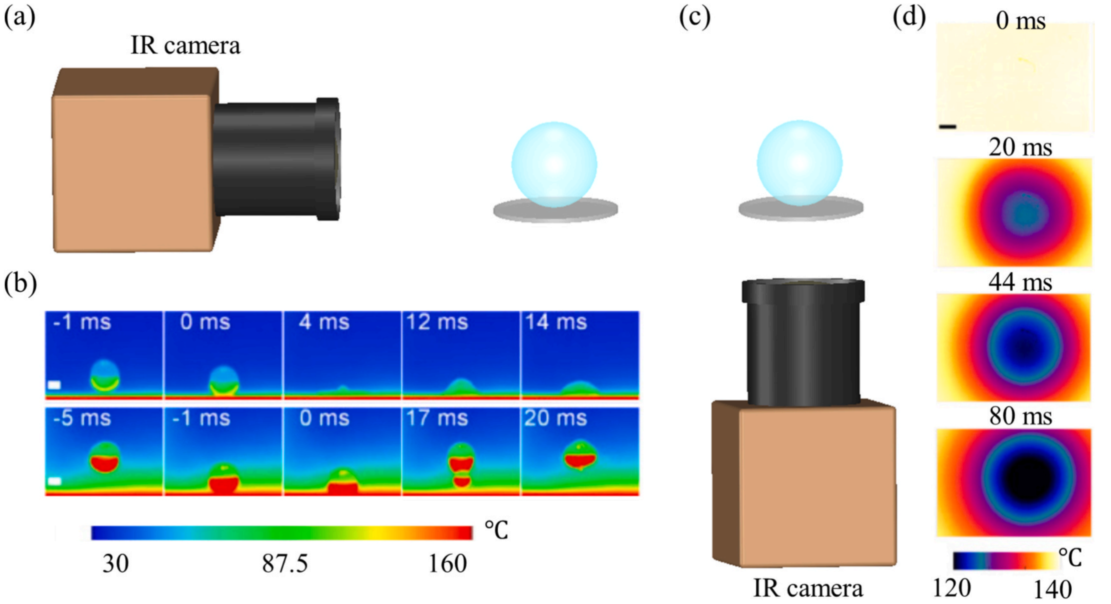

Fig. 8. Visualization of impinging droplet using IR camera. (a) Schematic of IR imaging from side view; (b) IR imaging sequences of impinging droplets obtained from the method described in (a) [98]; (c) Schematic of IR imaging from bottom view; (d) IR imaging sequences of substrate obtained from the method described in (c) [101]. The scale bars in (b) and (d) represent 1mm.

substrate [99–101,106,107], as shown in Fig. 8(c). To optimize the IR measurement accuracy in this configuration, the back side of the substrate is often coated with a black-body material to minimize reflections of surrounding infrared radiation [100]. The obtained thermal data enable the quantification of heat flux and energy transfer during droplet impact [99]. For instance, Li et al. used IR imaging to investigate the influence of surface physical modification on the heat transfer characteristics [101], as shown in Fig. 8(d). Their results demonstrated that engineered surface textures could enhance the heat transfer from the substrate to the impinging droplet, leading to an increase in the droplet's cooling capacity by up to 24% compared to an unmodified surface. Furthermore, IR imaging also provides valuable insights into the Leidenfrost effect, where a vapor layer forms between the droplet and a hot surface [108,109], and other interfacial thermal effects [107,109]. The ability to spatially and temporally resolve the interfacial temperature fields provides researchers a deeper understanding of the complex interplay between surface properties, fluid dynamics, and heat transfer during droplet impingement.

2.3. Numerical methods

Following the overview of experimental methods used to study drop impact dynamics, it is essential to discuss the various simulation methods (Fig. 9) that enhance our understanding of these phenomena. Simulation methods provide a means to explore and predict droplet behavior under different conditions, offering information that might be challenging to obtain through experimental investigations alone. Due to the symmetry of impact dynamics, 2D axisymmetric computations are commonly employed [50,110,111]. The momentum equation and the continuity equation for incompressible flow are given by the Navier Stokes equations:

$$\rho\frac{\partial \boldsymbol{u}}{\partial t}+\rho(\boldsymbol{u}\bullet\nabla)\boldsymbol{u}=\nabla\bullet\left[-\mathrm{P}\boldsymbol{I}+\mu\left(\nabla\boldsymbol{u}+\nabla\boldsymbol{u}^{\mathrm{T}}\right)\right]+\boldsymbol{F_g}+\boldsymbol{F_{st}} \tag{1}$$

$$\nabla\bullet\boldsymbol{u}=0 \tag{2}$$

where ρ and μ are fluid density and viscosity, t is time, $\boldsymbol{u}$ is the velocity vector, P is pressure, I is the identity tensor, $\boldsymbol{F_g}$ and $\boldsymbol{F_{st}}$ are gravitational and surface forces. The existence and deformations of the liquid–gas interfaces during drop impact process pose challenges for the accurate simulation. Several advanced computational techniques, such as the Level Set [112,113], Volume of Fluid (VOF) [114], Phase Field [115], Lattice Boltzmann methods [116], are widely employed for interface tracking. Each method has unique strengths and applications, supported by a variety of simulation software tools. The primary numerical simulation methods are outlined as follows.

2.3.1. Level set

The Level set (LS) method is a numerical technique used for tracking interfaces and shapes in computational fluid dynamics (CFD). This method represents the interface as the level set of a higher-dimensional scalar function, which evolves over time according to the underlying flow. The Level set function, ϕ, is typically governed by the advection equation [111,112,117]:

$$\frac{\partial\phi}{\partial t}+\boldsymbol{u}\bullet\nabla\phi=\varsigma\nabla\bullet\phi[\varepsilon_{ls}\nabla\phi-\phi(1-\phi)]\frac{\nabla\phi}{|\nabla\phi|} \tag{3}$$

where t is time, ς represent the reinitialization parameter of the level-set function, $\boldsymbol{u}$ is velocity vector, and ε_{ls} defines the thickness of the interface. ϕ smoothly varies between $0-1$ around the interface which is defined by $\phi = 0.5$. The surface tension force is calculated as $\boldsymbol{F_{st}} = \sigma\kappa\delta(\phi)\nabla\phi$, with κ being the curvature of the interface, $\delta(\phi)$ being the

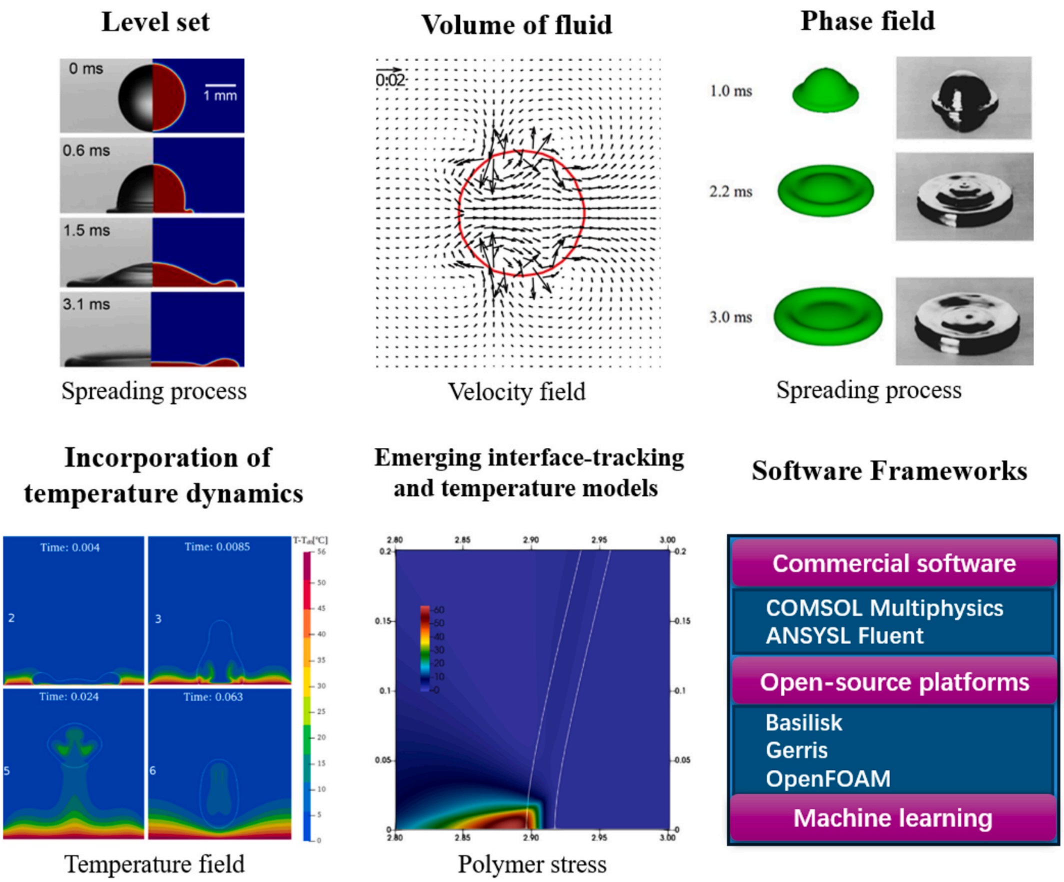

Fig. 9. Diverse numerical methods employed for simulation [120][128,131,134,147].

Dirac delta function, which is non-zero only on the interface. Finally, it provides a smooth and accurate representation of the interface, making it suitable for simulations involving intricate droplet dynamics, such as splashing [118]. A formulation for contact angle modeling can be incorporated into the LS method to accurately simulate droplet motion and energy evolution on diverse impact conditions [119–121]. However, mass conservation is a challenge using Level set method, as noted in prior studies [122–124].

2.3.2. *Volume of fluid*

The volume of fluid (VOF) method is another popular technique used to simulate multiphase flows, where the interface between fluids is captured by solving a volume fraction equation in each grid cell. The VOF method is governed by the equation for the volume fraction α [114]:

$$\frac{\partial\alpha}{\partial t}+\boldsymbol{u}\bullet\nabla\alpha=0 \tag{4}$$

where $\alpha=1$ and 0 represent the primary and the secondary fluids, respectively, and $0<\alpha<1$ indicates the interface. The surface tension force is incorporated as $\boldsymbol{F_{st}} = \sigma\kappa\nabla\alpha$, with $\kappa=\nabla\bullet\frac{\nabla\alpha}{|\nabla\alpha|}$ being the curvature of the interface [114,125].

The VOF method is known for its ability to conserve mass and track the interface between different phases, making it ideal for simulating energy evolution during impact process [51] and for long time scale dynamics, such as spreading and rebounding [50,126]. However, one of its key limitations lies in the fact that the interface is not explicitly defined. Instead, it must be reconstructed using strategies such as the Piecewise Linear Interface Calculation (PLIC) method [127]. While PLIC improves interface accuracy, differentiating the sharp volume fraction field can introduce significant errors, especially when calculating interface curvature or topologies [128].

2.3.3. *Phase field*

To address challenges with reconstructing sharp interfaces using VOF, alternative approaches like the Phase-Field Method provide a smoother interface, making them advantageous for solving complex interfacial phenomena. The Phase Field method introduces a continuous field variable, Θ, which distinguishes between different phases. The governing equation for the Phase Field method is the Cahn-Hilliard equation, coupled with the Navier-Stokes equations [129]:

$$\frac{\partial\Theta}{\partial t}+\boldsymbol{u}\nabla\Theta=\nabla\bullet\frac{y\lambda}{\zeta^2}\nabla\Psi \tag{5}$$

$$\Psi=-\nabla\bullet\zeta^2\nabla\Theta-\left(\Theta^2-1\right)\Theta \tag{6}$$

where Θ is the volume fraction of each phase that varies from -1 to 1, with $\Theta=-1$, $-1<\Theta<1$, and $\Theta=1$ being the gas, interface and liquid phases, respectively. $y=X\zeta^2$ is the phase-field mobility, and X is a mobility tuning parameter. λ is the mixing energy density. ζ determines the timescale of Cahn–Hilliard diffusion and was usually taken as half of the typical mesh size in the computational domain passed by the interface. In phase-field, the surface tension force is calculated as $F_{st} = G\nabla\Theta$, with $G = \lambda[-\nabla^2\Theta+\Theta\left(\Theta^2-1\right)/\zeta^2]$.

This method is highly effective in simulating complex interfacial phenomena, including phase transitions and capillary effects. Researchers successfully applied phase field method in drop impact dynamics, revealing the effects of various parameters including the Reynolds number, Weber number, density and viscosity ratios, and surface wettability on adherence, spreading and bouncing [129,130]. The Phase Field method is particularly useful for studying the thermodynamic aspects of droplet impact, such as solidification [131] and heat transfer [132]. But the determination of the mobility tuning parameter poses challenges for phase field method [133].

2.3.4. *Incorporation of temperature dynamics*

Since droplet impacts on heated surfaces involve strong coupling between fluid flow, phase transitions, and heat transfer, incorporating temperature dynamics into numerical simulations is essential. Each of the methods discussed in this section—Level-Set, Volume-of-Fluid, and Phase-Field—can be extended to include the effects of temperature by coupling the fluid dynamics equations with the heat transfer equation.

In the above methods, temperature dynamics are typically modelled by solving the advection–diffusion equation for temperature alongside the Navier-Stokes equations. The energy equation for temperature T can be written as [134]:

$$\frac{\partial T}{\partial t}+\boldsymbol{u}\bullet\nabla T=\nabla\bullet(\sigma\nabla T)+Q^{'} \tag{7}$$

where T is the temperature, σ is the thermal diffusivity, and $Q^{'}$ represents heat sources. This approach allows for the simulation of heat transfer across interfaces but may require additional corrections to account for phase changes [135].

2.3.5. *Emerging interface-tracking and temperature models*

Recent advances in numerical methods have focused on combining existing techniques to overcome individual limitations, improving the accuracy and robustness of simulations in complex multiphase systems. These hybrid approaches are particularly effective in capturing intricate interfacial dynamics, phase changes, and multiphysics interactions, such as solidification, freezing, boiling, and evaporation.

The hybrid phase field – volume of fluid (PFM-VOF) method provides a robust framework for simulating the three-dimensional binary solidification of alloys in the presence of gas bubbles [136]. This method combines the strengths of the diffuse phase field (ϕ) for tracking the liquid–solid interface and the sharp VOF method (ω) for capturing the gas–liquid interface. The combination ensures numerical stability while maintaining high accuracy in resolving interfacial dynamics.

The evolution of the gas–liquid interface is governed by [137,138]:

$$\frac{\partial\rho}{\partial t}+\nabla\bullet\rho\boldsymbol{u}=\rho\nabla\bullet\boldsymbol{u}-(\rho_l-\rho_s)(\frac{\partial\omega\phi}{\partial t}+\boldsymbol{u}\bullet\nabla(\omega\phi)) \tag{8}$$

where ρ_l and ρ_s are the densities of the liquid and solid phases, ω is the gas fraction, and volume fraction ϕ differentiates between liquid and solid phases in regions where $\omega > 0$. Specifically, $\phi = 0$ indicates a full liquid phase, $\phi = 1$ corresponds to a full solid phase, and $0<\phi<1$ indicates the presence of the liquid–solid interface. With mass conservation, there is

$$\nabla\bullet\boldsymbol{u}=\frac{\rho_l-\rho_s}{\rho}(\frac{\partial\omega\phi}{\partial t}+\boldsymbol{u}\bullet\nabla(\omega\phi)) \tag{9}$$

These equations enable the accurate modeling of density differences between solid and liquid phases, which are particularly important in scenarios involving freezing or phase change. The propagation of the solidification front is described by a modified Allen-Cahn equation [136,139]:

$$\begin{aligned}\tau_\beta\left(\frac{\partial\omega\phi}{\partial t}+\boldsymbol{u}\bullet\nabla(\omega\phi)\right)=\nabla\bullet\Bigg[\omega\Bigg(&W^2(\nabla\phi)\nabla\phi\\&+W(\nabla\phi)|\nabla\phi|^2\frac{\partial W(\nabla\phi)}{\partial\nabla\phi}\Bigg)\Bigg]-\omega f(\phi)-\lambda\omega r'(\phi)(\theta\\&+(MC_\infty U))\end{aligned} \tag{10}$$

Here τ_β is the kinetic coefficient relaxation time, ensuring that the phase field satisfies the Gibbs-Thomson relationship. The items in the right hand indicate different components of the Allen-Cahn equation, λ is employed to adjust the numerical thickness of the liquid–solid interface, $M=-\frac{m\left(1-k_p\right)}{\Delta T_0}$ is the dimensionless liquidus slope, with m as the dimensional liquidus slope, k_p as the partition coefficient, and ΔT_0 as the characteristic temperature.

This hybrid PFM-VOF method excels in capturing complex physical phenomena. For example, it can simulate dendritic growth, resolving anisotropic interfaces and interactions with gas bubbles or pores. It also supports thermal-solutal coupling, enabling accurate modeling of coupled temperature and solute transport during solidification. Furthermore, the method captures volume expansion by incorporating the effects of density differences during phase transitions such as freezing. These capabilities make the hybrid PFM-VOF method a powerful tool for studying multi-phase systems in applications ranging from metallurgy to cryogenics and icing phenomena.

The hybrid Volume of Fluid – Immersed Boundary Method (VOF-IBM) has been developed for simulating freezing processes in liquid films and drops. This versatile approach couples the VOF method—used to track the liquid–gas interface—with the IBM framework, which models the solidification front. The key advantage of this hybrid methodology lies in its ability to capture the complex interplay between heat transfer, phase change, and volume expansion due to density differences between liquid and ice. By incorporating surface tension and gravitational effects, the method provides a robust tool for analyzing freezing phenomena under diverse conditions. Validation against theoretical solutions and experimental observations demonstrates its accuracy and applicability to practical scenarios, including icing of surfaces and freezing drops with varying contact angles [140].

The coupling of VOF and IBM enables the accurate modeling of the solid–liquid–gas interface dynamics, where the VOF function (α) localizes the liquid–gas interface, and the IBM function (g) describes the ice fraction. The liquid–gas interface is governed by Eq. (4). Similarly, the ice fraction evolves according to:

$$\frac{\partial g}{\partial t}+\boldsymbol{v}_{s}\bullet\nabla g=0 \tag{11}$$

with $\boldsymbol{v}_s$ as the velocity of the solidification front. The physical properties such as density, viscosity, and thermal conductivity are expressed as 1-phase quantities, interpolated across the liquid, solid, and gas regions using the VOF and IBM functions. This interpolation ensures smooth variations in thermophysical properties across interfaces, improving numerical stability and accuracy. The governing equations for mass and momentum conservation account for the coupling between phase change and volume expansion. The mass conservation equation is given as:

$$\nabla\bullet\boldsymbol{u}=\alpha\left(1-\frac{\rho_{s}}{\rho_{l}}\right)\frac{\partial g}{\partial t} \tag{12}$$

where ρ_s and ρ_l are the densities of the solid and liquid phases, respectively. This equation ensures that the velocity jump at the solidification front is consistent with the density difference between the phases. The momentum conservation equation, based on the Navier-Stokes formulation, incorporates the effects of surface tension, gravity, and the IBM forcing term:

$$\rho\frac{\partial\boldsymbol{u}}{\partial t}+\rho(\boldsymbol{u}\bullet\nabla)\boldsymbol{u}=\nabla\bullet\left[-\mathrm{P}\boldsymbol{I}+\mu\left(\nabla\boldsymbol{u}+\nabla\boldsymbol{u}^{\mathrm{T}}\right)\right]+\boldsymbol{F_g}+\boldsymbol{F_{st}}+\boldsymbol{F_{IBM}} \tag{13}$$

where ρ and μ are fluid density and viscosity, t is time, $\boldsymbol{u}$ is the velocity vector, P is pressure, I is the identity tensor, and $\boldsymbol{F_{IBM}}=\chi\frac{\boldsymbol{u_s}-\boldsymbol{u}}{\Delta t}$ is the IBM forcing term.

The hybrid VOF-IBM method has been validated against theoretical solutions for the Stefan problem, showing excellent agreement in predicting the evolution of the solidification front. Grid and time convergence studies confirm the method's accuracy and efficiency, with errors decreasing as grid refinement and time step size improve. For freezing drops, the VOF-IBM method reveals the influence of contact angle, surface tension, and gravity on the freezing process. Drops with larger contact angles exhibit longer freezing times and distinct solidification front shapes, consistent with experimental observations. Additionally, the method accurately predicts the tip angle of frozen drops and the front-to-interface angle ($\approx 90^{\circ}$) under nearly adiabatic conditions, as reported in previous study [141]. This highlights the role of heat flux balance at the solidification front. Comparisons with experimental data further validate the method's ability to reproduce the final shape of frozen drops and their internal temperature and velocity distributions. These results demonstrate the hybrid VOF-IBM method's capability to model complex freezing phenomena across a wide range of conditions.

Wang et al. [142] introduced a binary fluid Cahn-Hilliard-Navier-Stokes (CHNS) system to model the interaction of droplets with solid substrates. In the phase-field approach, the interface between two immiscible fluids is represented implicitly by a diffuse transition layer, where the phase-field variable (ϕ) varies smoothly between the two phases ($\phi = -1$ for one phase and $\phi = 1$ for the other). The interface itself is identified as the region where ϕ transitions from -1 to $+1$, with the interface thickness controlled by the Cahn number (Cn). In addition to ϕ, the model introduces a second variable, ψ, which represents the surfactant concentration as a fraction ranging from 0 to 1. The surfactant modifies the interfacial tension and plays a critical role in the dynamics of the interface. The distribution of ψ evolves according to the Cahn-Hilliard equation, which describes the dynamics of both ϕ and ψ under the influence of advection, diffusion, and interfacial effects.

The evolution of ϕ, which governs the interface dynamics, is given by:

$$\phi_{t}+\nabla\bullet\boldsymbol{u}\phi=\frac{1}{Pe_{\phi}}\Delta\eta_{\phi} \tag{14}$$

where $\boldsymbol{u}$ is the velocity field, Pe_ϕ is the Péclet number, and η_ϕ is the chemical potential derived from the total free energy. The surfactant concentration ψ evolves according to:

$$\psi_{t}+\nabla\bullet\boldsymbol{u}\psi=\frac{1}{Pe_{\psi}}\nabla\bullet M_{\psi}\nabla\eta_{\psi} \tag{15}$$

where $M_\psi = \psi(1-\psi)$ is the degenerate mobility [143]. Pe_ψ is the Péclet number for surfactant transport, and η_ψ is the chemical potential for ψ. The chemical potential η_ϕ is given by:

$$\eta_{\phi}=-Cn^{2}\Delta\phi+\phi^{3}-\phi+\frac{1}{Ex}\psi\phi-\psi(\phi^{3}-\phi) \tag{16}$$

and for the surfactant concentration η_ψ:

$$\eta_{\psi}=Pi\ln\left(\frac{\psi}{1-\psi}\right)+\frac{1}{2\mathrm{Ex}}\phi^{2}-\frac{1}{4}(\phi^{2}-1)^{2} \tag{17}$$

where ψ represents the surfactant concentration, Pi is the temperature-dependent constant, and Ex determines the bulk solubility. These equations couple the dynamics of the fluid interface (ϕ) and surfactant concentration (ψ), allowing the model to capture surfactant-induced changes in interfacial tension and Marangoni effects. Unlike methods that explicitly track sharp interfaces (e.g., VOF or Level-Set), the phase-field approach embeds the interface dynamics directly into the governing equations. This eliminates the need for explicit interface reconstruction or tracking, enabling the model to naturally handle complex phenomena such as topology changes (e.g., merging, breakup) and surfactant adsorption. The model also incorporates the generalized Navier boundary condition (GNBC) to account for moving contact lines on solid substrates, ensuring thermodynamically consistent dynamics. The momentum equation in the CHNS system, which describes the fluid flow, is given as [144]:

$$\rho\left(\frac{\partial\boldsymbol{u}}{\partial t}+\boldsymbol{u}\cdot\nabla\boldsymbol{u}\right)+\nabla p=\frac{1}{Re}\nabla\cdot(\mu\boldsymbol{D}(\boldsymbol{u}))-\frac{1}{WeCn}(\phi\nabla\mu_{\phi}+\psi\nabla\mu_{\psi}) \tag{18}$$

where ρ is the density, μ is the viscosity, Re and We are the Reynolds and Weber numbers. By utilizing the phase-field representation, this model provides a robust and flexible framework for simulating droplet impact dynamics. It has been shown to accurately capture adherence, bouncing, and splashing phenomena, as well as the influence of surfactant-induced Marangoni effects on interfacial behavior.

Accurate interface tracking is essential for modeling boiling and evaporation flows, as the interface separates liquid and gas phases where mass, momentum, and energy exchange occur. A novel approach was introduced that combines the Volume of Fluid method with an embedded boundary method (EBM) to maintain interface sharpness and ensure the conservation of mass, momentum, and energy [33,145,146]. The geometrical VOF method represents the liquid–gas interface as a sharp boundary, avoiding numerical diffusion. The evolution of the liquid volume fraction α is also governed by the advection equation, i.e., Eq. (4). The interface is reconstructed geometrically at each timestep to preserve its sharpness, ensuring consistent updates to properties such as density (ρ) and viscosity (μ) in interfacial cells. Material properties are updated using:

$$\phi = \phi_{liq}\alpha + \phi_{vap}(1-\alpha) \tag{19}$$

where ϕ represents a general material property such as density or viscosity. Implemented within the finite volume (FV) framework, this approach ensures conservation across computational cells and is particularly effective for high-resolution simulations of complex phase change phenomena.

The embedded boundary method further enhances the accuracy of interface tracking by dividing interfacial cells into liquid and gas regions, allowing for precise enforcement of jump conditions. During phase change, the mass flux across the interface is given by:

$$\dot{m} = \rho_l(\boldsymbol{u}_{int} - \boldsymbol{u}_l)\cdot\mathbf{n} = \rho_v(\boldsymbol{u}_{int} - \boldsymbol{u}_v)\cdot\mathbf{n} \tag{20}$$

where $\mathbf{n}$ is the normal vector at the interface, and subscripts l and v refer to the liquid and vapor phases, respectively. This leads to the velocity jump condition:

$$[\mathbf{u}\cdot\mathbf{n}]_{int} = (1/\rho_v - 1/\rho_l)\dot{m} \tag{21}$$

The thermal flux across the interface is computed as:

$$q = -k\nabla T\cdot\mathbf{n} \tag{22}$$

where k is the thermal conductivity. To ensure continuity, the temperature gradient (∇T) is calculated separately in the liquid and gas regions using second-order interpolation schemes. Similarly, the vapor concentration flux is governed by:

$$\dot{m} = \frac{(\rho D_m \nabla Y)_v\cdot\mathbf{n}}{1 - Y_{int}} \tag{23}$$

where D_m is the diffusion coefficient of vapor. These sharp schemes allow the model to accurately enforce interfacial jump conditions without smearing scalar fields, avoiding numerical artifacts and maintaining physical authenticity.

Zhao et al. [145] introduced a robust coupling of temperature (T) and vapor concentration (Y) fields at the interface. The mass flux due to phase change is determined by both the temperature gradient and the vapor concentration gradient through the interface:

$$\dot{m} = \frac{(\lambda\nabla T)_l - (\lambda\nabla T)_v}{L} = \frac{(\rho D_m \nabla Y)_v\cdot\mathbf{n}}{1 - Y_{int}} \tag{24}$$

where L is the latent heat of vaporization. The interfacial temperature (T_{int}) is further coupled to the vapor pressure (P_{sat}) through the Clausius-Clapeyron equation:

$$P_{sat} = P_{atm}\exp\left(-\frac{h_{lg}M_v}{R}\left(\frac{1}{T_{int}} - \frac{1}{T_{sat}}\right)\right) \tag{25}$$

where M_v is the molar mass of vapor, R is the gas constant, and T_{sat} is the saturated temperature. This thermodynamic coupling enables the model to capture complex phase change dynamics, such as boiling and evaporation, even in challenging scenarios like the Leidenfrost effect, where both processes occur simultaneously in different interfacial regions.

The model was validated against several benchmark problems, including the sucking problem, bubble growth in superheated liquid, and droplet evaporation under forced convection. In the Leidenfrost problem, the model successfully simulated the rebounding behavior of a droplet above a superheated surface, accurately resolving the thin vapor film and coupling effects between boiling and evaporation. These validations demonstrate the robustness and versatility of the model for capturing dynamic interfacial phenomena with strong phase change effects. By combining sharp interface tracking with conservative numerical schemes, the model effectively resolves vapor generation, heat transfer, and interfacial dynamics. Unlike smeared-interface methods, the embedded boundary method enforces interfacial jump conditions without artificial smoothing, ensuring accurate modeling of phase change dynamics. These strengths make the VOF-EBM model a powerful tool for direct numerical simulations (DNS) of multiphase flows with phase change.

Simulating two-phase flows with sharp interfaces is a critical challenge, particularly in systems involving viscoelastic fluids and moving contact lines. The study by Bazesefidpar et al. [147] addresses this challenge by introducing a dual-resolution phase-field solver that combines computational efficiency with high accuracy. The solver employs the Cahn-Hilliard phase-field model to capture the interface dynamics and incorporates viscoelasticity using the Giesekus model. This approach is particularly well-suited for simulating droplet wetting, deformation, and motion across solid surfaces, which are influenced by surface tension, viscoelastic stresses, and dynamic contact angles.

The phase-field method replaces the sharp interface between two immiscible fluids with a diffuse interfacial region, where the phase-field variable ϕ transitions smoothly between $\Theta = 1$ (fluid 1) and $\Theta = -1$ (fluid 2). This transition is governed by the Cahn-Hilliard equation:

$$\frac{\partial\Theta}{\partial t} + \nabla\cdot(\boldsymbol{u}\Theta) = \nabla\cdot(M\nabla G) \tag{26}$$

where $G = \lambda(-\nabla^2\Theta + f(\Theta))$ is the chemical potential, M is the mobility parameter, and $f(\Theta) = \frac{1}{\eta^2}\Theta(\Theta^2 - 1)$ is a function derived from the mixing energy density. The parameter λ controls the interfacial tension in the sharp-interface limit, while ξ defines the diffuse interface thickness. A critical advantage of this method is its ability to handle topological changes, such as droplet breakup or coalescence, without requiring explicit interface tracking. To resolve the flow dynamics, the solver couples the Cahn-Hilliard equation with the Navier-Stokes equations for incompressible flow:

$$\rho\frac{\partial\boldsymbol{u}}{\partial t} + \rho(\boldsymbol{u}\bullet\nabla)\boldsymbol{u} = \nabla\bullet\left[-\mathrm{P}\boldsymbol{I} + \mu\left(\nabla\boldsymbol{u} + \nabla\boldsymbol{u}^{\mathrm{T}}\right)\right] + \boldsymbol{F_g} + \boldsymbol{F_{st}} + \nabla\cdot\tau \tag{27}$$

subject to the incompressibility condition $\nabla\bullet\boldsymbol{u} = 0$. Here, ρ and μ are the phase-dependent density and viscosity, interpolated across the interface. Additional complexity arises from the inclusion of viscoelasticity, modeled using the Giesekus constitutive equation:

$$\tau_p + \lambda_H\left(\frac{\partial\tau_p}{\partial t} + u\cdot\nabla\tau_p - \tau_p\nabla u - \nabla\boldsymbol{u}^T\tau_p\right) + \alpha\lambda_H\mu_p(\tau_p\cdot\tau_p) = \mu_p(\nabla u + \nabla\boldsymbol{u}^T) \tag{28}$$

where τ_p is the polymeric stress tensor, λ_H is the relaxation time, μ_p is the polymeric viscosity, and α is the Giesekus mobility parameter. The relationship between the polymeric stress and the conformation tensor cc is given by:

$$\tau_p = \frac{\mu_p}{\lambda_H}(c - I) \tag{29}$$

ensuring that viscoelastic effects are accurately represented even under high deformation rates. Dynamic wetting is modeled by coupling the phase-field variable with a dynamic contact angle condition at the solid wall. This condition enforces the relaxation of the dynamic contact angle toward the equilibrium static contact angle. This formulation allows the solver to capture the interplay between surface wettability, fluid elasticity, and interface motion.

A key innovation of this method is the dual-resolution strategy, which resolves the phase-field variable Θ on a finer grid than the velocity, pressure, and polymer stresses. The finer grid ensures that the diffuse interface is well-resolved, while the coarser grid reduces the computational cost associated with solving the Navier-Stokes and viscoelastic stress equations. This approach is particularly advantageous for three-dimensional simulations, where the computational cost typically scales with the cube of the grid resolution. The coupling between the fine and coarse grids is achieved through interpolation and restriction operations. For example, velocities are interpolated from the coarse grid to the finer grid to solve the Cahn-Hilliard equation, while phase-field variables are averaged back to the coarser grid to update fluid properties. This ensures consistent coupling between the two grids without compromising accuracy. The dual-resolution solver was validated against several benchmark problems, demonstrating its robustness and accuracy. The solver was also applied to dynamic wetting problems, such as the spreading of Newtonian and viscoelastic droplets on solid substrates. The equilibrium droplet shapes and spreading radii matched analytical predictions and experimental data, confirming the model's ability to handle contact-line dynamics. Notably, the dual-resolution approach achieved a computational speed-up of more than 2× compared to single-resolution simulations, while maintaining the same level of accuracy.

2.3.6. Software frameworks: commercial, open-source & thermal applications

The numerical methods discussed above are implemented using a variety of computational tools. Commercial software such as COMSOL Multiphysics and ANSYS Fluent are popular for their accessibility and user-friendly interfaces, while open-source platforms like Basilisk and Gerris are valued for their flexibility and advanced features, such as adaptive meshing. Although the mathematical models (Sections 2.3.1–2.3.5) are methodologically universal, their implementation within different software platforms is tailored to address specific scenarios in droplet impact research. This implementation plays a critical role in determining accuracy, scalability, and thermal coupling effectiveness. This section provides a comparative analysis of key computational frameworks used in droplet impact research, highlighting their strengths and limitations in the context of thermal engineering.

Some commercial software has been successfully employed for simulating drop impact dynamics. These commercial software packages support Level-Set, Volume of Fluid, and phase Field methods, making them suitable for complex multiphase flow simulations. The dynamics of droplet spreading, including velocity fields, energy distribution, and maximum spreading coefficients, have been effectively studied using COMSOL with the Level-Set method [120,148]. Building on this approach, Nguyen et al. investigated the transient thermocapillary migration of a small liquid droplet on a horizontal solid surface [149]. Lunkad et al. employed the VOF method in ANSYS Fluent to analyze droplet impact and spreading, demonstrating that static contact angle models are effective for hydrophobic surfaces, whereas dynamic contact angle models are crucial for hydrophilic surfaces due to higher initial contact angles [126]. Similarly, Blake et al. utilized ANSYS Fluent with a coupled Volume-of-Fluid and Level-Set method to study the impact and solidification of supercooled water droplets on cooled substrates, concluding that the timescale of the initial stage of solidification is negligible to the overall simulation outcome.

In addition to these tools, open-source platforms like Basilisk and Gerris have gained significant traction in the research community for fluid dynamics and multiphase flow simulations. Basilisk utilizes adaptive mesh refinement to efficiently resolve complex fluid interfaces and dynamic changes in flow fields, providing a flexible framework for implementing custom physical models [150]. For example, Li et al numerically investigated droplet impact dynamics on micropillar-arrayed soft surface using Basilisk [151]. Their work involved VOF method to simulate complex multiscale interactions between droplets and micropillared substrates. They revealed that splash intensity increased with higher impact velocity and ambient pressure, while it decreased with higher surface tension. Wei et al employed Basilisk to implement PFM-VOF and achieved to capture the propagation of solidification bounded by the liquid/gas interface. Gerris is renowned for its adaptive quadtree/octree grid structures, which allow for high spatial and temporal resolutions of droplet impact dynamics. Jian et al utilized Gerris with a VOF-based interface tracking method to explore the splashing mechanism [110]. Their results confirmed the dominant gas effect on the droplet spreading dynamics and demonstrated two different splashing mechanisms. Similarly, Philippi et al. employed Gerris and the VOF method to reveal a short-time self-similar structure in both the velocity and pressure fields during the early stages of droplet impact. They found that the pressure peaked near the contact line, not at the center, and that the contact line exhibited a tank-treading motion [152]. OpenFOAM, another powerful open-source tool, has been widely adopted in the research community for simulating complex fluid dynamics problems [153]. Unlike Basilisk and Gerris, which specialize in adaptive mesh refinement, OpenFOAM provides a highly customizable framework based on finite volume methods (FVM) [154]. It is designed to handle a wide range of multiphysics problems, including heat transfer, turbulence, and multiphase flows. For example, Samkhaniani et al. [134] extended the phase-field method in OpenFOAM to incorporate interfacial heat transfer and the thermal Marangoni effect. They investigated the hydrodynamics and heat transfer of droplets impinging on heated hydrophobic surfaces and found that the Weber number primarily governs heat transfer, with higher values increasing wetted areas, thinning liquid films, and improving cooling effectiveness. Marangoni forces further enhanced spreading, contact time, and heat transfer with both the surface and air. Schremb et al. [155] investigated non-isothermal droplet impacts onto cold surfaces using a VOF-based model in OpenFOAM, extended to include conjugate heat transfer. Their parametric study revealed that the minimum droplet temperature depends primarily on the substrate temperature, while the total heat transfer is influenced by the contact time and wetted area, which are determined by the impact velocity and droplet size. More recently, Gu et al. [125] used a 2D VOF model in OpenFOAM to study droplet impacts on microstructured surfaces, revealing that high Weber numbers increased impact forces. Bead size, spacing, and air cushions significantly influenced splashing and fragmentation. These findings provide valuable insights for optimizing surface design to control droplet impact dynamics, benefiting applications such as erosion protection, microfluidics, and thermal engineering systems. Overall, commercial software like ANSYS Fluent can not only be used for specific industrial applications, offering robust prebuilt models and user-friendly interfaces, but also serve as a valuable tool in research due to its reliability and extensive validation. In contrast, open-source platforms such as Basilisk provide greater flexibility, allowing researchers to modify the code, implement custom physics, and investigate cutting-edge or emerging phenomena. This adaptability makes open-source tools particularly suited for academic research and the exploration of novel or complex multiphase flow scenarios.

In recent years, machine learning and data-driven approaches have also been integrated into simulation workflows to enhance the accuracy and efficiency of droplet impact simulations [156,157]. The two approaches make use of large datasets generated from experiments and simulations to create predictive models that can rapidly estimate droplet behavior under different conditions. Dickerson et al employed machine learning based on preliminary experimental results to predict the impact behavior on concave targets [158]. Such techniques are becoming increasingly valuable in optimizing simulation parameters and reducing computational costs.

3. Boiling regimes and impact dynamics

3.1. Impact phenomena on non-heated surfaces

When a droplet encounters a solid surface, various physical phenomena appear. Upon contact, the initial impact stage involves the rapid deformation and spreading of the droplet, driven by the balance of inertial, capillary, and viscous forces. This stage can be characterized by the formation of a dimple at the bottom of the droplet [159], the capillary wave [89], and the expanding lamella [160,161]. The subsequent behavior of the impinging object is influenced by the surface and droplet properties, such as the surface wettability, the droplet surface tension and the viscosity.

On a surface with a temperature below the saturation point, the impacting droplet may undergo deposition, bubble entrapment, partial rebound, and complete rebound (as shown in Fig. 10, depending on the surface wettability and the balance of the aforementioned forces. It has been proved that the wettability of the surface plays a crucial role in determining the final state of the impacting droplet. Highly wettable surfaces promote the spreading and deposition of the droplet, while less wettable surfaces can facilitate droplet receding and rebound after spreading process [17]. Another important phenomenon observed in droplet impact on non-heated surfaces is splashing, where the impacting droplet breaks up into smaller secondary droplets. The splashing consists of corona splash and prompt splash. In the corona splash, the secondary droplets are ejected from the expanding lamella that is separated from the substrate and have a crown-like structure. Corona splash is commonly observed on smooth surfaces [160,162]. By contrast, the prompt splash is characterized by the ejection of small droplets directly from liquid-substrate contact line that generally occur on rough surfaces [161,163]. The occurrence and characteristics of splashing are influenced by a multitude of factors. The threshold of splashing occurrence can be characterized by a non-dimensional parameter, splash number, $K = We^{1/2}Re^{1/4}$. When the splash number is beyond a critical value $K_C \approx 57$, a splashing can be expected [160,164]. Higher impact velocities and larger droplet sizes lead to larger K and thus promote splashing, as the inertial forces overcome the capillary forces. The role of viscous forces in splashing is more complex. For low-viscosity droplets, viscous forces can destabilize the liquid and promote splashing by enhancing the breakup of the expanding lamella [165]. Conversely, for high-viscosity droplets, viscous forces act to suppress splashing by damping the inertial energy and stabilizing the liquid interface [166,167]. This reversed role of liquid viscosity on splashing highlights the intricate interplay of inertial, viscous, and capillary forces in determining the splashing threshold.

Except intrinsic properties of droplet, external factors also have nontrivial effects on splashing occurrence. Xu et al. have found that by decreasing the air pressure, the splashing can be significantly suppressed, as show in Fig. 11(a). Later, they further distinguished the effects of gas pressure on corona splash and prompt splash. On smooth surfaces, corona splash occurs and can be suppressed by the decease of the gas pressure; while on rough surfaces, where prompt splash occurs, the gas pressure shows less suppression effects (Fig. 11(b)). Goede et al. and Laka et al. found that splashing threshold is independent of the wetting properties of the surface [168,169]. But their investigated surfaces were limited within hydrophilic surfaces. Zhang et al. later expanded this investigation to include a wider range of surface wettability, from hydrophilic to hydrophobic. They found that the splashing threshold does indeed depend on the surface wettability. The critical

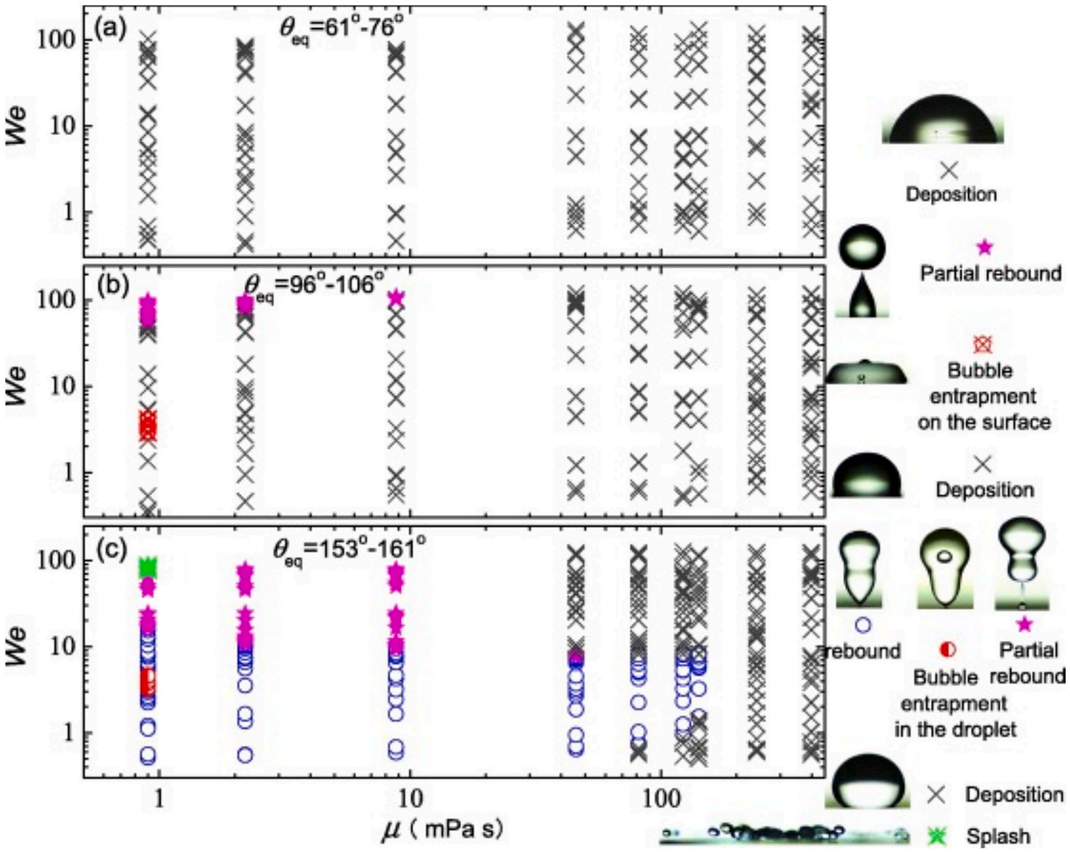

Fig. 10. Phase diagram of impact phenomena as a function of the Weber number and liquid viscosity. (a) On lyophilic surfaces with contact angle $\theta_{eq} \approx 61^\circ - 76^\circ$; (b) on lyophobic surfaces with $\theta_{eq} \approx 96^\circ - 106^\circ$; (c) on superhydrophobic surfaces with $\theta_{eq} \approx 153^\circ - 161^\circ$ [17].

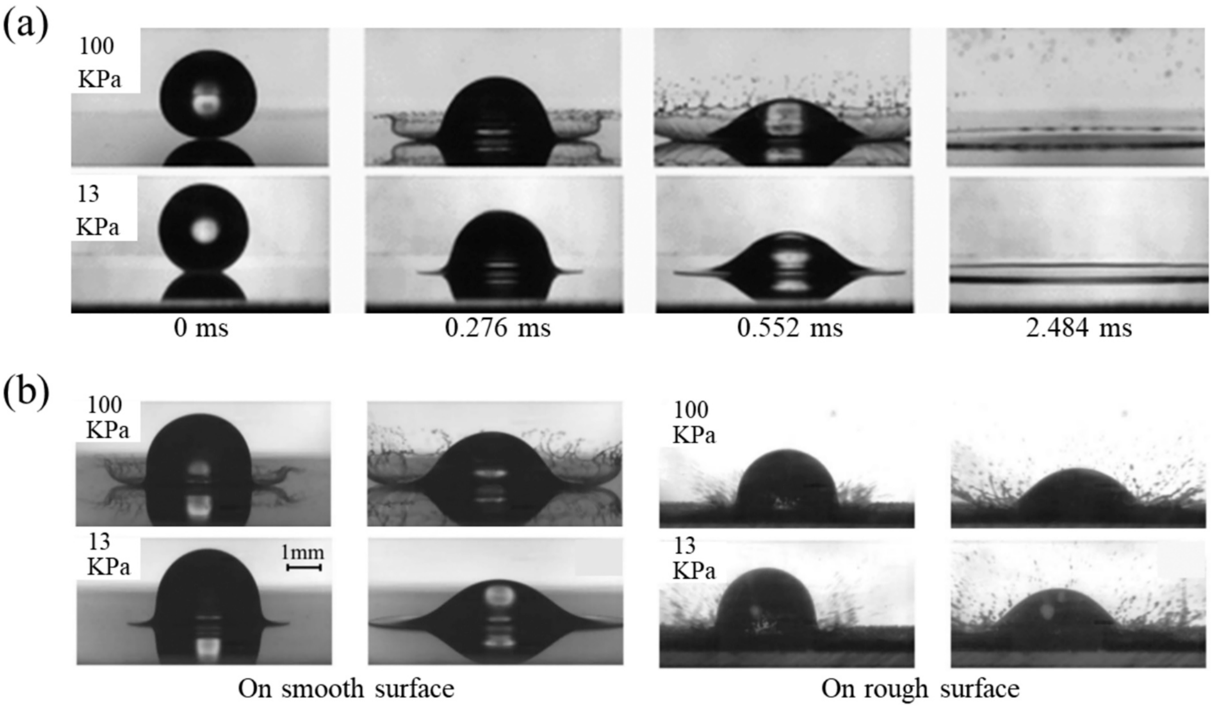

Fig. 11. Splashing occurrence. (a) Sequential snapshots of splashing occurrence on smooth surfaces [162]; (b) splashing occurrence as a function of gas pressure and surface roughness [163].

splash number is independent of surface wettability for surfaces with $\theta_a < 90^\circ$, but decreases as θ_a increases when $\theta_a > 90$, where θ_a is the advancing contact angle [164]. The behind mechanism can be ascribed to the increase of the lift force on the expanding lamella on surfaces with $\theta_a > 90^\circ$ [164].

3.2. *Impact phenomena on heated surfaces*

3.2.1. *Boiling regimes*

The interaction dynamics of droplet impact are critically influenced by the relative temperature difference between the substrate (T_w) and liquid boiling temperature (T_B). While droplet impingement on superheated surfaces ($T_w > T_B$) might suggest immediate vaporization, the initiation of boiling exhibits complex temperature-dependent behavior governed by transient thermal coupling between the droplet and substrate [31,106]. The heat transfer mechanisms dominated by transient conduction during initial contact evolving to convective heat transfer during spreading progressively elevate liquid temperature without immediate phase change at moderate superheats. The initial liquid–gas interface demonstrates extreme instability. The duration of this unstable behavior is closely correlated with the surface temperature, surface structure, and physical properties of the droplet [75]. Two fundamental boiling modes govern post-impact dynamics: nucleate boiling characterized by discrete bubble formation, and film boiling marked by sustained vapor layer formation [31]. These regimes create distinct hydrodynamic responses that can be systematically categorized through three critical temperature thresholds: Boiling temperature (T_B), Transition temperature (T_{Tr}), Leidenfrost temperature (T_L). Fig. 12(a) [170] demonstrates how these thresholds delineate four characteristic regimes: non-boiling deposition ($T_w < T_B$), nucleate boiling deposition ($T_B \le T_w < T_{Tr}$), transition boiling rebound ($T_{Tr} \le T_w < T_L$), and Film boiling rebound ($T_w \ge T_L$). Recent classifications [16,171] further distinguish these dynamics as: stable deposition, thermal dancing, vapor-induced atomization, and complete rebound.

High-Weber number impacts introduce additional complexity through splashing phenomena [172], while temporal evaporation characteristics enable regime identification through lifetime analysis (Fig. 12(b) [31]). This classification aligns with classical boiling curve fundamentals [173,174], though Yang et al. [175] proposed an innovative refinement differentiating “standing” and “floating” film boiling states based on partial droplet adhesion. Fig. 13 provides regime-specific thermal deformation patterns as follows: (a) Film evaporation: Characterized by conduction-dominated heat transfer through wall-film convection [176], exhibiting a morphology analogous to ambient impacts [21]. (b) Nucleate boiling: Features localized superheat vaporization generating bubble nucleation cycles. The resultant micro-convection enhances heat flux, facilitating thermal atomization which is crucial for spray cooling applications. (c) Transition boiling: Marked by vapor–liquid instability producing macro-scale droplet fragmentation. Distinct from inertial splashing, this regime generates polydisperse secondary droplets through vapor collapse events. (d) Leidenfrost regime: The sustained formation of a vapor film creates thermal insulation, enabling droplet levitation. The study in [175] elucidates the intricate dynamics of the vapor layer that influence the bouncing kinematics via thermocapillary effects. Furthermore, when the oscillation of the droplet induces parametric resonance in the vapor layer, the system transitions from “floating” or bouncing states to exhibit a trampolining behavior [177], In this state, upon each successive contact with the heated surface, the droplet bounces to greater heights [178]. These temperature-dependent regime classifications provide critical insights for thermal management applications, particularly in optimizing spray cooling performance through nucleate boiling enhancement while avoiding Leidenfrost-induced heat transfer deterioration.

3.2.2. *Vapor layer in the Leidenfrost regime*

The Leidenfrost regime features a self-sustaining vapor layer that thermally decouples impacting droplets from the heated substrate. Upon contact with surfaces exceeding the Leidenfrost temperature, instantaneous vaporization at the liquid–solid interface generates a quasi-stable vapor film, which levitates the droplet while drastically suppressing heat transfer compared to nucleate or transition boiling regimes, this vapor-mediated levitation arises from a dynamic balance between upward

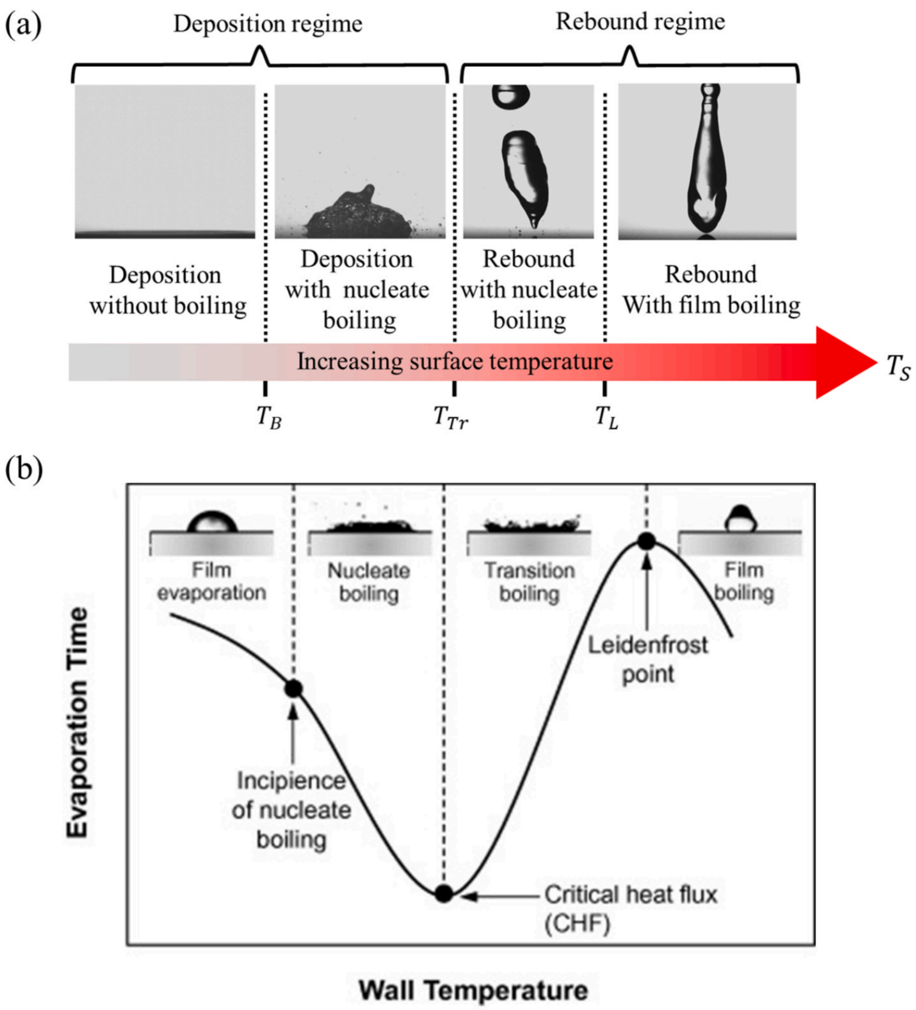

Fig. 12. Hydrodynamics and heat transfer regimes associated with a droplet impinging a heated surface. (a) Hydrodynamics regimes. T_B: Boiling temperature; T_{Tr}: Transition temperature; T_L: Leidenfrost temperature [170]; (b) Heat transfer regimes based on boiling curve [31].

lubrication forces F_{Lu} and gravitational effects. Theoretical models [180,181] correlate F_{Lu} can be calculated by

$$F_{Lu} = 12\pi\mu_a \int_0^R \overline{v_r} r^2 / h^2 \mathrm{d}r \tag{7}$$

where μ_a is the air viscosity, $\overline{v_r} = \dot{q}r/2h$ is the horizontal radial velocity in the vapor layer, $\dot{q}$ is the flow rate, ρ_v, k, L, and ∇T are the vapor density, thermal conductivity, the latent heat of evaporation, and temperature gradient, respectively. r is the radial position from the droplet center, and h is the thickness of the vapor layer.

Quantitative characterization of vapor layer morphology reveals scale-dependent behavior. Biance et al. [180] demonstrated via side-view imaging that vapor film thickness scales with droplet radius R_0, following $h \sim 0.01\ R_0$ (h ranging 10μm −100μm at 1 mm $< R_0 <$ 8 mm) (Fig. 14(a)). Advanced interferometric techniques [182,183] further resolved submicron spatiotemporal variations in δ, unveiling temperature-independent vapor pocket geometry below critical substrate temperatures ($T_w \leq 370$ °C; Fig. 14(b-c)). These studies established that vapor layer topology is governed primarily by hydrodynamic constraints rather than thermal driving forces in moderate superheat conditions. Recent breakthroughs in synchrotron X-ray imaging have enabled direct visualization of vapor layer microstructures under extreme superheats. Lee et al. [184] observed distinct vapor layer profiles for ethanol droplets: parallel vapor films dominated at $T_w < 420$ °C, while elevated temperatures ($T_w > 420$ °C) induced center-peaked vapor geometries due to intensified thermocapillary flows (Fig. 14(d)). This temperature-dependent morphological transition accentuates the complex interaction between droplet and vapor layer stabilization, which might be a consideration for high-temperature applications involving low-viscosity fluids.

3.3. *Effect of surface temperature on dynamic variables*

3.3.1. *Maximum spreading*

The maximum spreading diameter (β_m) of impacting droplets, a critical determinant of interfacial transport efficiency, exhibits distinct temperature-dependent behavior across boiling regimes. While classical scaling laws $\beta_m \sim We^a$, $\beta_m\ Re^a$ governed by inertial-capillary-viscous balance dominate sub-boiling temperatures ($T_w < T_B$) [43,160], superheated surfaces induce fundamentally altered spreading mechanisms: In non-boiling regime, spreading kinematics remain comparable to ambient conditions, with viscous dissipation and surface tension playing secondary roles to inertial forces. Experimental studies demonstrate minimal β_m variation for water (Fig. 15(a) [185]) and ethanol [186] droplets despite T_w increases, though viscosity-sensitive fluids show enhanced spreading through reduced viscosity. In transition regime, emerging vapor nucleation creates counteracting effects—localized boiling enhances liquid mobility while vapor cushioning inhibits contact-line advancement. This competition produces non-monotonic $\beta_m(T_w) \sim Re(T_d)^{1/4}$ behavior, ultimately reducing maximum spread

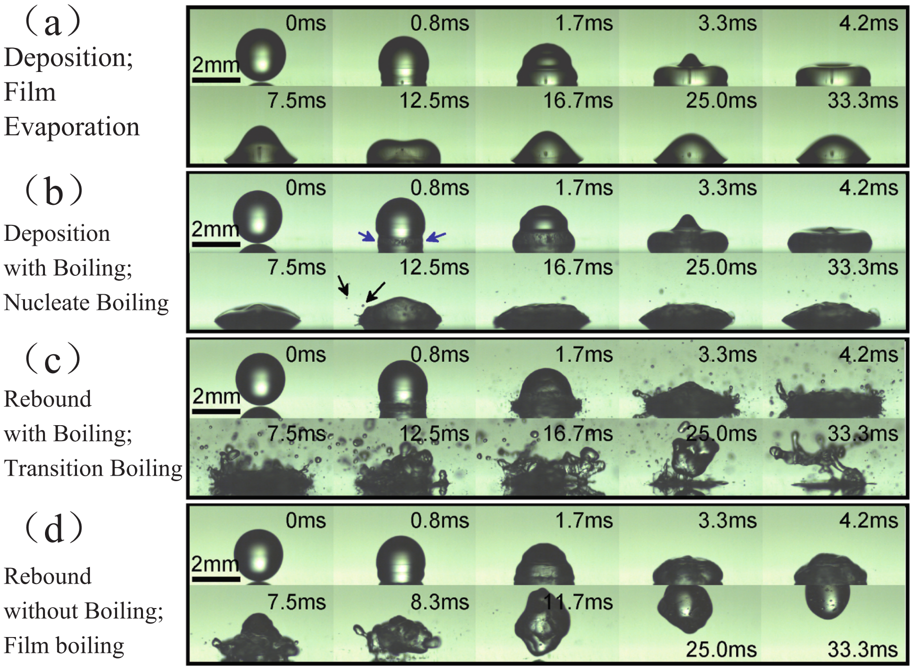

Fig. 13. Thermally induced droplet deformation in four regimes after impact onto heated surfaces with temperature 100 °C (a), 160 °C (b), 220 °C (c) and 300 °C (d) [179].

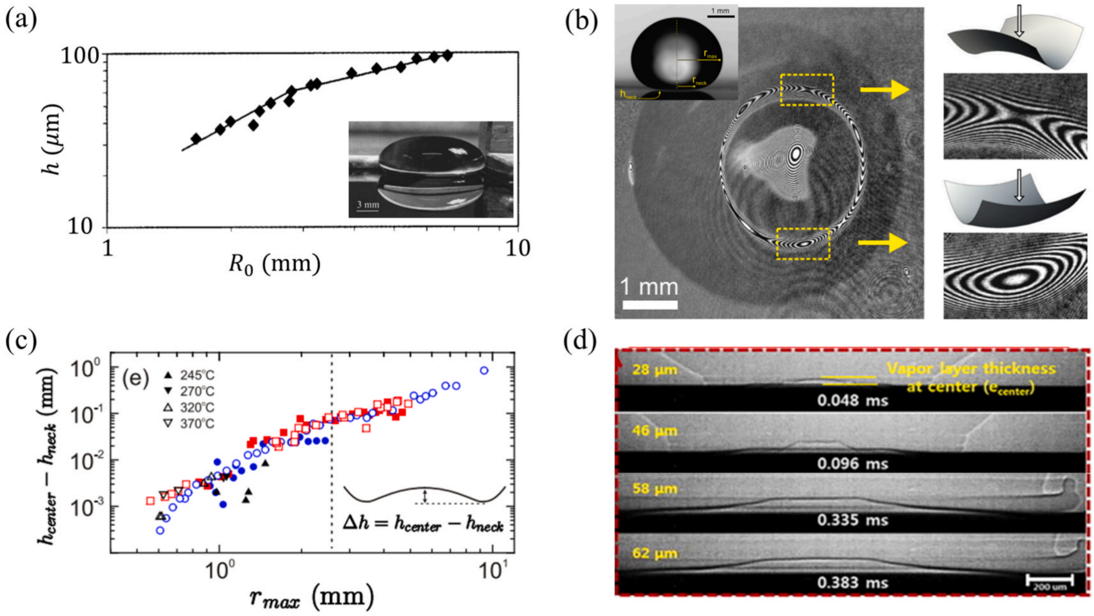

Fig. 14. Vapor layer in the Leidenfrost regime. (a) Thickness of the vapor layer beneath a water droplet as a function of droplet radius R_0 [180]; (b) bottom-view interference image beneath a water Leidenfrost drop [182]; (c) thickness of the vapor layer as a function of droplet flatten radius $r_{\max}$ [182]; (d) side-view images of vapor layer captured by synchrotron X-ray [184].

below Leidenfrost thresholds [185,186]. In Leidenfrost Regime, Vapor-mediated levitation decouples β_m from thermal effects (Fig. 15(b)), yielding universal scaling relationships: $\beta_m \sim We^{2/5}$ (smooth surface [187]), $\beta_m \sim We^{3/10}$ (structured surfaces [188,189]), the elevated exponents compared to superhydrophobic surfaces ($We^{1/4}$) originate from vapor-jet-driven radial momentum transfer during film boiling [187].

For adaptations of complex fluids, polymer additives introduce elastic stress dominance, shifting to $\beta_m \sim We^{1/2}$ scaling [190–192]. Low-boiling-point fluids adhere to $\beta_m \sim (We/Oh)^{0.143}$, highlighting the modulation of viscous-thermal coupling by the Ohnesorge number ($Oh = \mu/(\rho\sigma D_0)^{0.5}$) [193]. Dual scaling emerges with $\beta_m(T_s) \sim Re(T_d)^{1/4}$ (low μ) transitions to $\beta_m(T_s) \sim Re(T_d)^{1/5}$ (high μ) for different Ionic Liquids, reflecting the development of the viscosity-governed thermal boundary layer [194]. Liquid metals (LMs) [195], such as Gallium-based alloys, exhibit a characteristic maximum spreading scaling of $\beta_m \sim We^{1/2}$, analogous to viscoelastic polymer solutions. Unlike polymers, however, LMs could maintain this relationship without droplet atomization even under extreme superheating, which is a consequence of their intrinsically high boiling points. Their distinctive spreading behaviour stems from the formation of self-

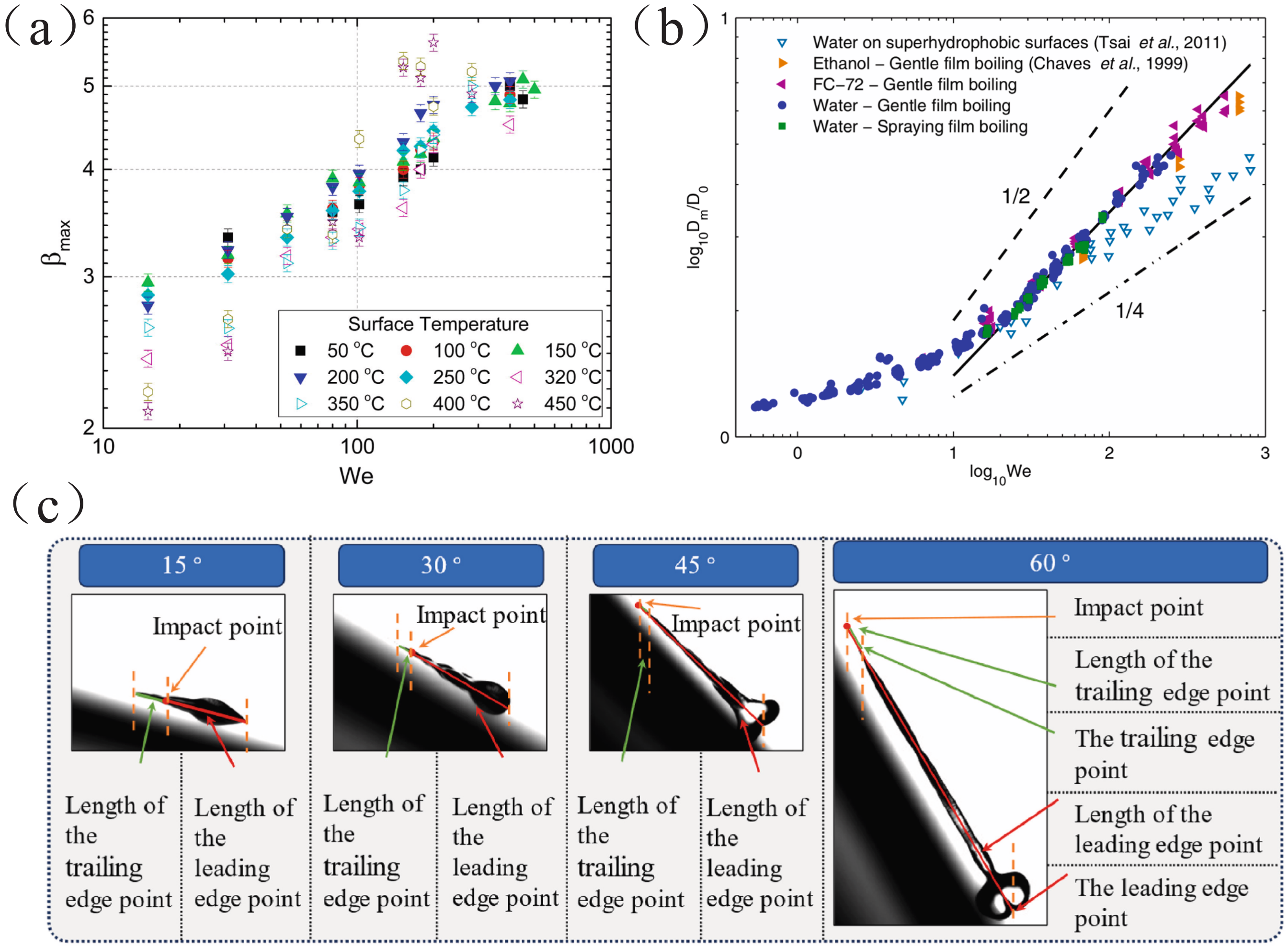

Fig. 15. (a) Maximum spreading factors of water droplet impacting on porous surface [185]; (b) Maximum spreading factors of water and fluorine droplets impacting on silicon wafers [187]; (c) Water droplets impacting on an inclined heated surface [197].

limiting oxide skin at air–liquid interfaces [196], a process that occurs within milliseconds upon atmospheric exposure. This oxide layer gives rise to dynamic interfacial tension gradients, which crucially regulate the spreading kinematics. The dynamics of droplet impact on an inclined surface constitute yet another distinct scenario. As illustrated in Fig. 15 (c), the spreading of the droplet on the inclined surface is intricately intertwined with the inclination angle, height, and temperature. The spreading diameter on the inclined surface is characterized by the lengths of the leading and trailing edge points. The maximum spreading diameter can be calculated using the formula $A\beta^3_{tmax} + B\beta^2_{tmax} + C\beta_{tmax} + E = 0$, where β_{tmax} denotes the tangential maximum spreading factor, A, B, C and E are four coefficients of in one variable cubic equation function of the normal Weber number, the normal Reynolds number, and the inclination angle.

3.3.2. Splash threshold

The surface temperature of the substrate can have a significant effect on the splash threshold, as it can alter the underlying physical mechanisms governing the droplet impact and breakup dynamics. The splash threshold undergoes temperature-dependent transitions governed by competing interfacial phenomena across two characteristic regimes. Elevated surface temperatures suppress splashing through thermal modulation of ambient gas dynamics, when the surface temperature is below T_{Tr}. As demonstrated in Fig. 16(a) [172,198], an increasing surface temperature reduces aerodynamic lift forces on expanding lamellae compared to ambient conditions. This suppression mechanism is quantitatively captured by the thermal adaptation of the Riboux – Gordillo (R&G) model [199].

The suppression effects are also found on rough surfaces; however, the impact of surface roughness tends to reduce the extent of this suppression. As shown in Fig. 16(b), the variations of the critical splash number on rougher surfaces (defined by the root-mean-square roughness R_q) exhibit a less steep gradient. By integrating an additional force term originating from surface roughness into the R&G model, one can account for the combined effects of surface temperature and roughness on the splash threshold [170]. Later, Tao et al. [200] further established a universal scaling relationship between the critical Weber number and the surface roughness, $We_c \propto R_q^b$, revealing a decreasing exponent magnitude (b: 2.2 → 0.2) with increasing roughness due to amplified flow instability generation counteracting air evacuation effects (Fig. 16 (c-d)). Above T_{Tr}, the formation of a vapor layer at the liquid–solid interface fundamentally alters the mechanics of splash initiation. The emergent vapor cushion reduces solid–liquid adhesion, leading to a sudden decrease in the splash threshold [170,172]. This regime shift highlights the transition from aerodynamically dominated to vapor-mediated splash dynamics.

4. Surface topography and wettability

4.1. Roughness and texture

The impact dynamics of droplets on heated surfaces are governed by

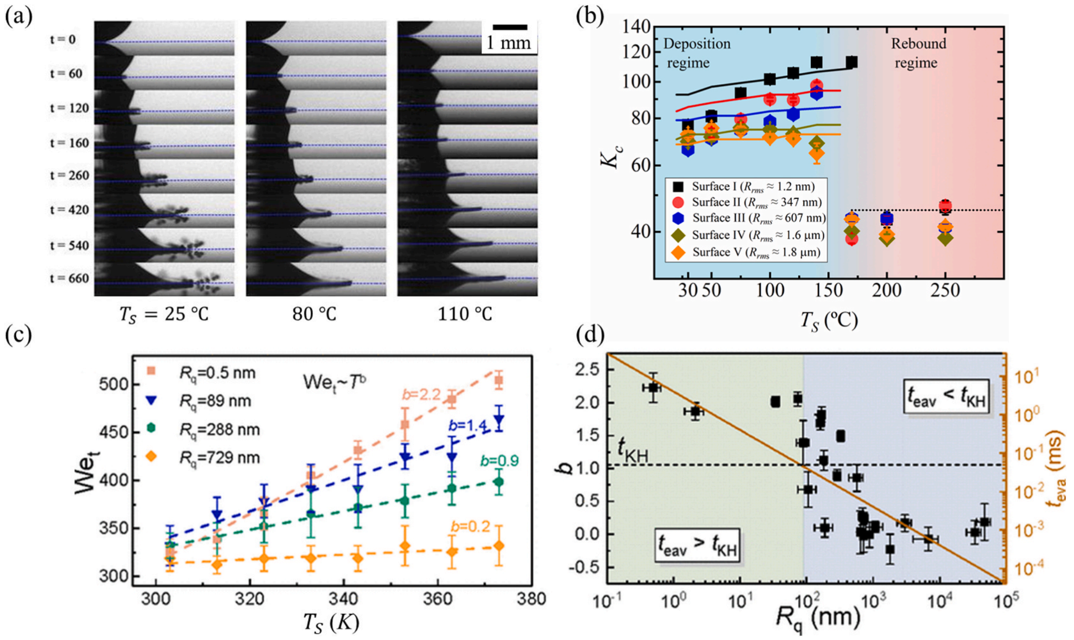

Fig. 16. Effects of surface temperature (T_S) on splashing. (a) Snapshots of splashing process on surfaces with different T_S [198]; (b) variation of critical splash number K_c as a function of surface temperature and surface roughness [170]; (c) variation of critical Weber number (We_T) as a function of T_S on different rough surfaces, which shows $We_T \propto T_S^b$ [200]; (d) the exponent b as a function of surface roughness R_q [200].

interfacial interactions between liquid properties and surface characteristics, including roughness [170], texture [201–203], wettability [204,205], and thermal conditions. Compared to smooth surfaces [187,206], micro/nanostructured surfaces [35,188,207] substantially modify phase diagrams through amplified interfacial effects. The formation of a thermally insulating vapor layer beneath the droplet – the Leidenfrost effect [208,209]- induces droplet rebound, with the Leidenfrost temperature T_L and transition temperature T_{Tr} serving as critical thresholds between deposition and rebound regimes. As shown in Fig. 17(a), surface roughness induces a monotonic decrease in both T_L and T_{Tr} attributable to enhanced thermal transport at rough interfaces. Concurrently, the critical splash number exhibits temperature-dependent growth with diminishing sensitivity at elevated roughness levels. Notably, T_L demonstrates dual dependencies: it increases with surface roughness for fixed materials while decreasing with thermal diffusivity for constant roughness [210], as illustrated in Fig. 17(b). To quantify these effects, a criterion $\delta_c \gtrsim \delta_c^* + S_a$ is proposed to account for linear influence of surface roughness on the critical film thickness requisite for the stabilization of the Leidenfrost state. However, on the surface of the micropillars, the effect of the surface roughness on T_L diminishes beyond a certain critical interpillar spacing (~200 μm). This is because the excess vapor gap in the Leidenfrost state depends on the permeability of the substrate and affects the temperature range that sustains transition boiling [211]. When the texture spacing is decreased below a critical small value (~10 μm) which represents a minimum T_L [212], the emergence of this critical value can be attributed to instability-driven mechanisms and the increase in surface area. Consequently, the design of the surface texture allows for the modulation of the interactions between droplets and heated surfaces.

For instance, porous architectures [32,213–216], micropillars arrays [201,202,217–219], and hierarchical structures exert profound thermodynamic control over droplet-surface interactions. Systematic investigations of textured surfaces reveal: woven meshes exhibit T_L from 265 °C (0.004 mm^2 open area) to 315 °C (0.1 mm^2) [220]. SiO_2 nanoparticle-coated hierarchical textures [32] achieve $T_L > 490$ °C, representing a 178 °C enhancement over bare stainless steel, as depicted in Fig. 17(c). Micropillars can increase T_L by approximately 270 °C and reach approximately 507 °C compared to a smooth surface [211]. Engineered surfaces enable non-equilibrium phenomena like pancake bouncing through rapid capillary energy rectification [221]. Fin-array-like micropillars enable inertial vapor bubble growth at 130 °C, inducing momentum-driven droplet jumping via thermal boundary layer engineering [219], as shown in Fig. 17(d).

4.2. Wettability

Wettability-mediated droplet dynamics display temperature-dependent bifurcations, as depicted in Fig. 17(e). While substrate wettability minimally affects impact forces on unheated surfaces [222], heated systems (surface temperature from 125 °C to 415 °C and Weber numbers from 10 to 225) reveal distinct atomization behaviors [204]: persistent atomization below T_L on hydrophilic/superhydrophilic surfaces, absence of atomization at low Weber numbers and low excess surface temperatures on hydrophobic surfaces, and quasi-Leidenfrost suspension with vapor escape on superhydrophobic interfaces. The Leidenfrost state paradoxically combines heat transfer suppression (stable levitation) with potential enhancement strategies [220]. Partial wetting states ($\theta_{eq} \approx 110^\circ$) demonstrate 390 % heat flux augmentation through surface-adherent "standing" droplets [175], while microratchet geometries enable directional droplet propulsion governed by aspect ratio-dependent thrust [223,224].

On a heated superhydrophobic surface, adhesion becomes nonmeasurable even at moderate temperatures; the transition to the suspended Leidenfrost state occurs continuously with increasing temperature, and the superhydrophobic structure maintains the stability of the vapor layer down to the liquid's boiling point, thereby giving rise to a "cold Leidenfrost regime" [225], as shown in Fig. 18(a–c). In this state, although the droplets bounce higher at elevated temperatures, they can still rebound at room temperature. This is because superhydrophobic surfaces, characterized by Cassie-Baxter wetting states ($\theta_{eq} > 150^\circ$) [226], display unique droplet rebound behavior. This behavior stems from air-entrapping micro/nanotextures that minimize solid–liquid contact [227]. Moreover, surface heating enhances this behavior, reducing the contact time ($\tau \sim \sqrt{\rho D_0^3/\sigma}$) through accelerated retraction dynamics [1,192].

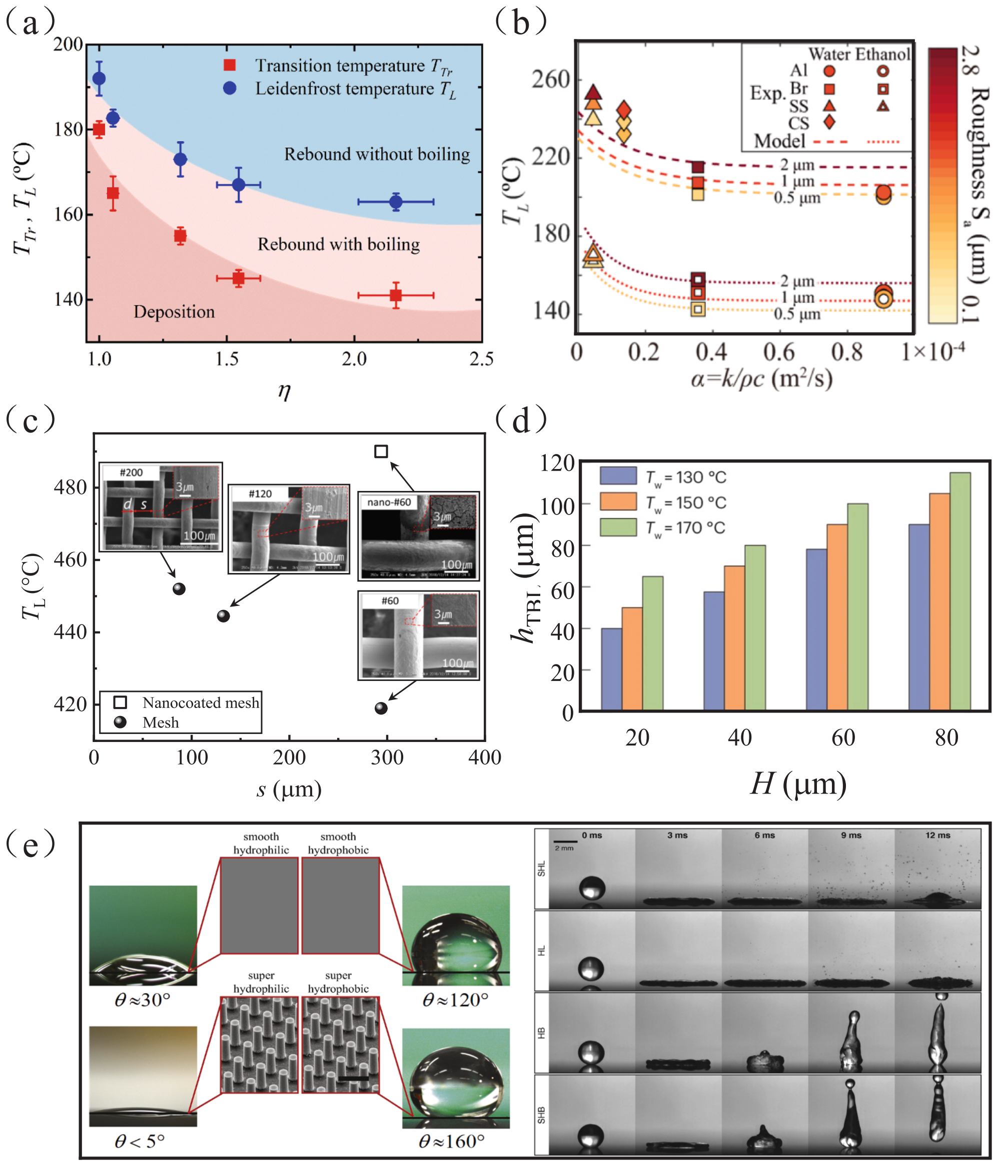

Fig. 17. Effect of surface roughness (a-b) [170,210], texture (c-d) [32,219] and wettability (e) [204] on variation of the Leidenfrost temperature or jumping behaviors.

As the temperature exceeds the boiling point of the liquid, the adhesion diminishes further. Droplets will continuously bounce on the heated surface and ultimately detach from the superhydrophobic surface. Nevertheless, when there are changes in the physical properties of the liquid, such as an increase in concentration, this bouncing behavior will be inhibited, as depicted in Fig. 18(d) [192], and the adhesion force will assume a dominant role. These findings underscore the pivotal significance of fluid physical properties and surface wettability engineering for accurate thermal management. In the later section, the impact of fluid physical properties on impact dynamics will be elaborated upon in detail. Nevertheless, it is of utmost significance to note that superhydrophobic surfaces encounter challenges related to poor mechanical stability, which restricts their engineering applications. The domain of superhydrophobic surfaces has drawn considerable attention in recent years, with a variety of reviews concentrating on different aspects of their fabrication and applications [228–230]. Fabrication techniques encompass manipulation of nano-roughness [231], plasma technology [232], corrosion control [233], self-healing [234], and other strategies [235,236]. Therefore, enhancing their stability and durability constitutes a crucial research direction, such as an effective strategy for reinforcing the mechanical stability of the superhydrophobic surface by embedding water-repellent nanostructures within a protective microstructure ’armour’ [237].

4.3. Applications via surface engineering

The dynamics of droplet impact on heated surfaces is of crucial significance across a wide range of applications. Prominent applications encompass thermal dissipation and energy conversion. These representative applications leverage two counterintuitive strategies via surface engineering: suppressing rebound to prolong liquid–solid contact and enabling controlled rebound for rapid droplet renewal. With reference to the Leidenfrost temperature, these applications can be classified into two additional groups: (1) Increasing T_L and (2) reducing T_L [38]. For example, spray cooling, particularly crucial for high heat-flux electronics [7], primarily utilizes rebound inhibition mechanisms where surface modifications amplify heat transfer through convection enhancement via wall film flow modulation, intensified evaporation at extended three-phase contact lines, and capillary-driven liquid imbibition in porous/nanofibrous media. As aforementioned, three

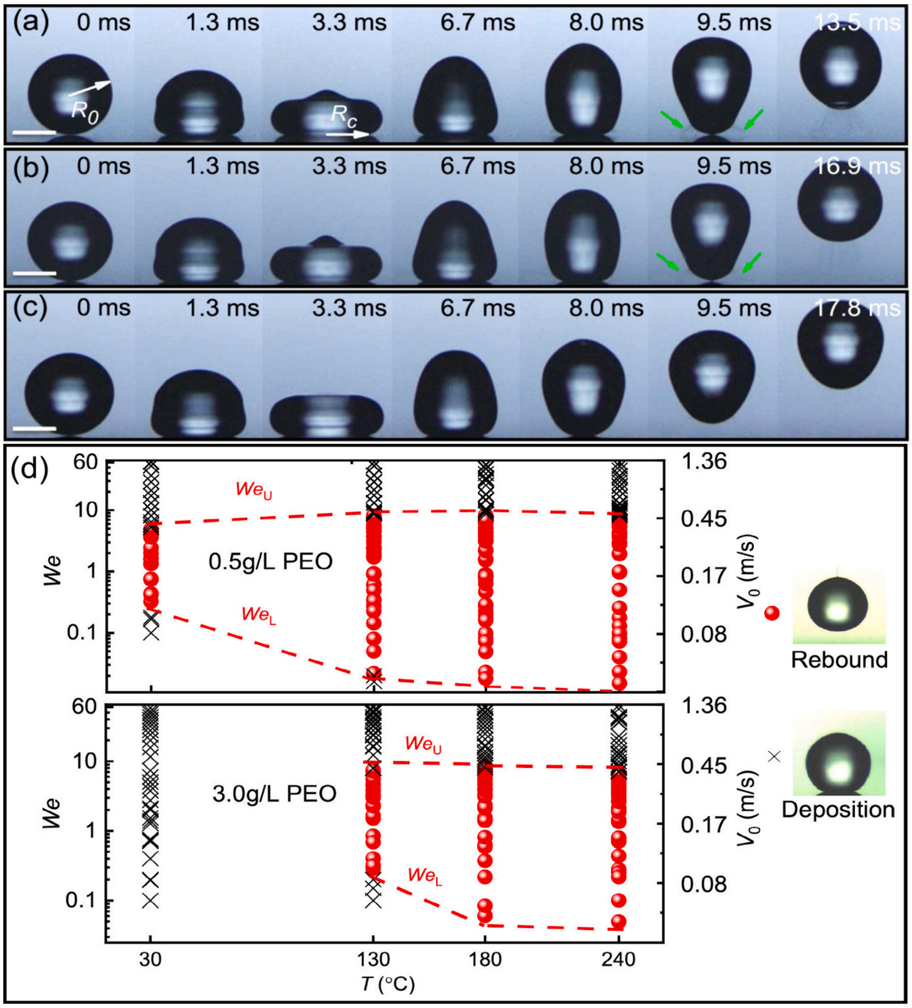

Fig. 18. Snapshots of impinging droplets of aqueous polymer solution on superhydrophobic surfaces at 25 °C (a), 50 °C (b), 95 °C (c), and impact phase diagram at higher temperatures [1,192].

.

representative surface architectures show exceptional performance: Wettability-patterned surfaces, micro/nano-scale arrays, and Hierarchical structures. For instance, superhydrophilic wedges on superhydrophobic substrates enable directional droplet drainage [238], 100–200 μm porous coatings achieve 62 % heat flux enhancement relative to the plain surface [239], and hybrid micro-nanotextures boost critical heat flux (CHF) by 110 % through multiscale phase change optimization [240].

The Leidenfrost temperature manipulation presents a critical challenge in ultrahigh-temperature spray cooling (>1000 °C). Recent advances address the gas drainage-vapor generation paradox through interfacial oscillation control and structured thermal armors (STA). STA, e.g., micropillar arrays with U-shaped vapor channels suppress Leidenfrost effect up to 1150 °C via embedded insulating superhydrophilic membranes, active vapor evacuation during liquid imbibition [109], as shown in Fig. 19(a). While these surface engineering strategies have significantly improved the efficiency of spray cooling by suppressing droplet rebound, there are other techniques that modify the surface to enable controlled rebound for rapid droplet renewal. For instance, recent progress has demonstrated multifunctional integration on superhydrophobic-pyroelectric generators [241]. The TiO_2 NPs-coated surface achieve over threefold power density enhancement at 80 °C through Weber number-modulated spreading (Fig. 19(b)). Rapid droplet rebound holds another significant potential for application on surface deep fouling. During the process of droplet rebound, fouling, even in surface roughness and cavities, can be effectively purged in a deep – cleaning fashion, as reported in reference (Fig. 19(c)) [219].

5. Dynamics of complex fluid droplets

5.1. Recent advances of non-Newtonian fluids

The post-impact hydrodynamics of droplet-surface interactions are primarily governed by three interrelated parameter clusters: (1) fluidic properties encompassing density–viscosity-surface tension relationships, (2) kinematic parameters defined by Weber-Reynolds-Ohnesorge numbers, and (3) substrate characteristics involving wettability modulation and thermophysical gradients. Additional parameters must be considered when external physical fields are applied, as exemplified by ferrofluid droplets under a magnetic field [242]. Ferrohydrodynamic interactions typically show asymmetric spreading due to variations in the magnitude of the Lorentz force [243], which causes the droplet to preferentially spread in a direction orthogonal to the magnetic field lines. The application of a magnetic field facilitates the onset of Rayleigh-Plateau droplet pinch-off, while magneto-visco-capillarity governs the suppression of droplet rebound [244]. This section further synthesizes current understanding of complex fluid droplet dynamics during surface impingement, building upon Phalguni and Michelle [245] taxonomic framework that distinguishes particulate suspensions and polymeric fluids. This classification illuminates distinctive

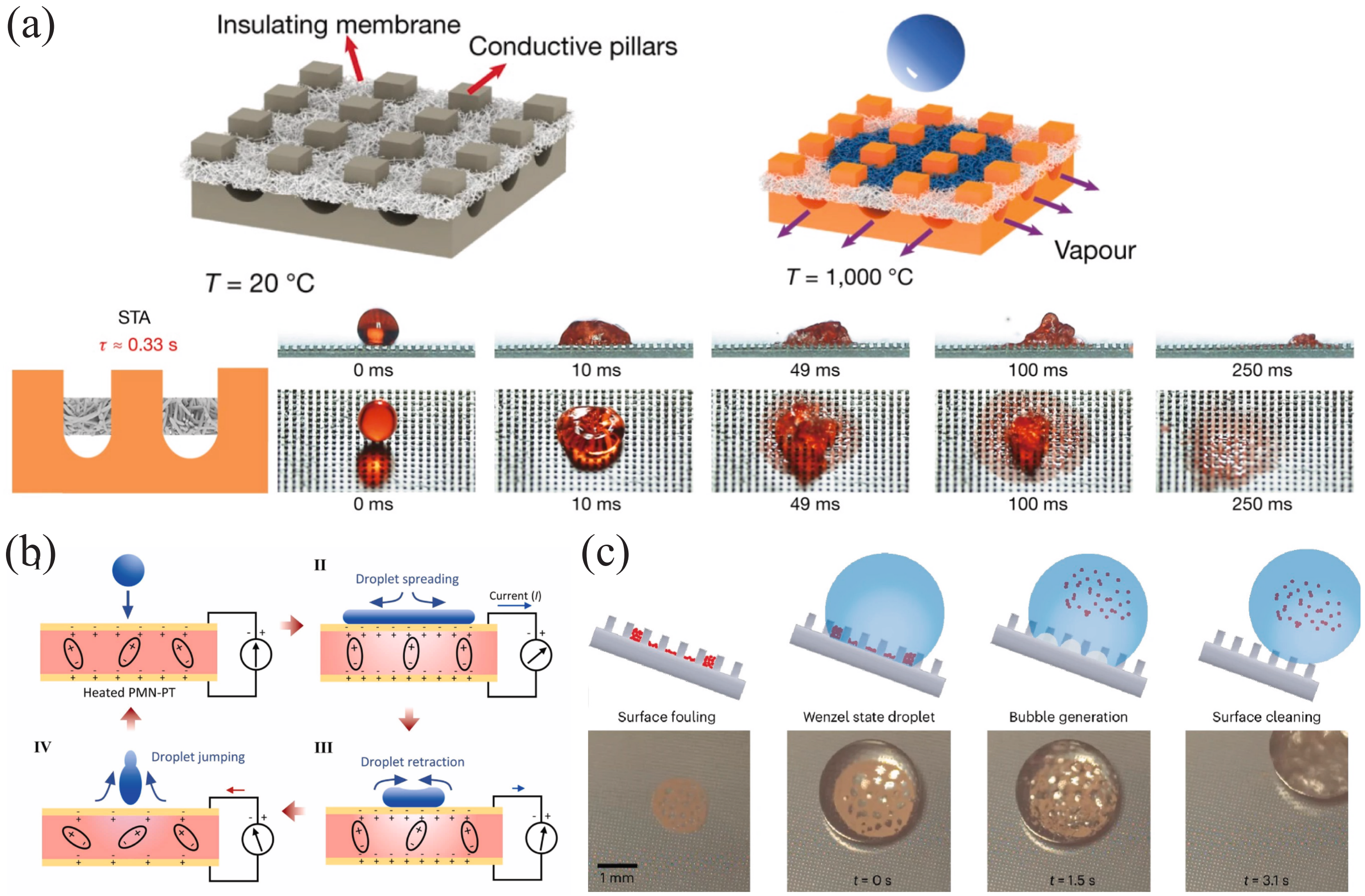

Fig. 19. Typical applications achieved through surface engineering. (a) Leidenfrost effect inhibited by the structured thermal armour (STA) above 1,000 °C, adapted from [109], (b) High-powered superhydrophobic pyroelectric generator via droplet impacting on heated surface and working principle during droplet impact, adapted from [241], (c) Surface deep fouling occurs via the process of droplet rebound [219].

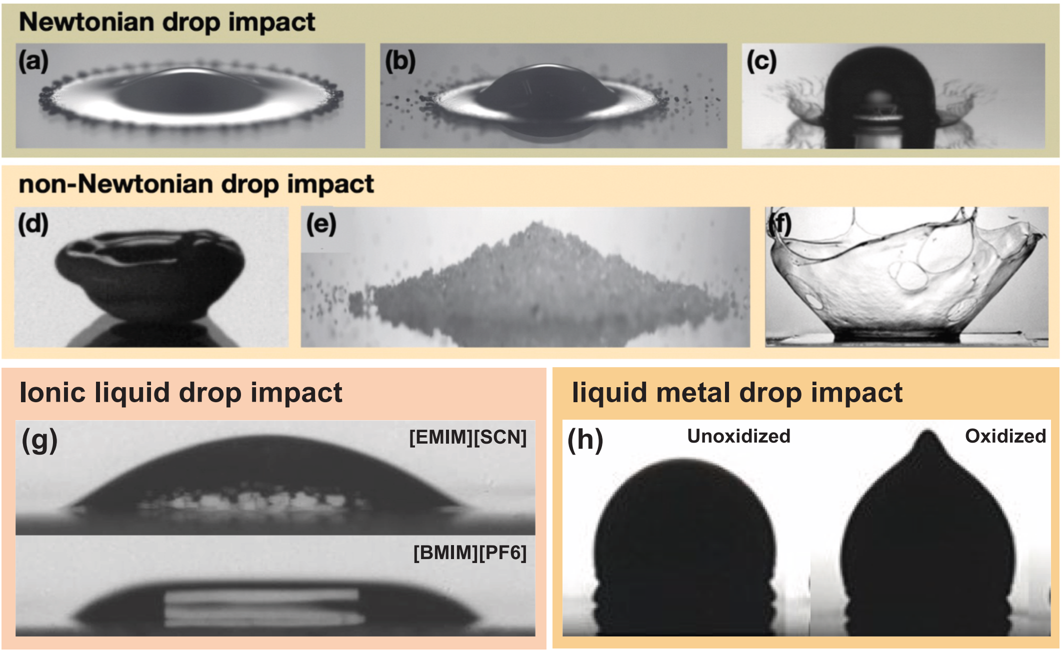

Fig. 20. Impact phenomenon for representative Newtonian (a–c) and non-Newtonian (d-f) fluids, ionic liquid (g), liquid metal (h), adapted from [194,245,252]
.

hydrodynamic behaviors under dynamic free-surface conditions. Particulate suspensions exhibit binary behavior based on particle size regimes: Brownian suspensions (nanoparticle-laden fluids) and non-Brownian systems (micron-scale particles). A recent comprehensive review [246] elucidates their impact dynamics on heated substrates, revealing unique spreading-splashing characteristics. Notably, nanofluids demonstrate exceptional promise for advanced droplet/spray cooling applications through their tailored thermal properties. During spreading, Newtonian fluids exhibit canonical splashing modes (Fig. 20 (a-c)), while non-Newtonian droplets manifest anomalous behaviors including solidification-induced rigidity, retarded spreading kinetics, and splashing suppression (Fig. 20(d-h)). Aqueous polymeric droplets, which exhibit non-Newtonian behavior, are primarily influenced by two key parameters: polymer concentration [191] and Weissenberg number. Polymer concentration determines the relaxation timescale, while the Weissenberg number quantifies both the elastic effects of polymer chains and the hydrodynamic forces, thereby defining the regime for the onset of rebound suppression [247]. Regarding rebound suppression on superhydrophobic surfaces, there exist two concurrent mechanisms:: the role of Cassie to Wenzel transformation or impalement serves as necessary conditions [248]. These mechanisms are strongly correlated with droplet impact outcomes, highlighting the importance of incorporating rheological characterization into impact models. Elastic, water-filled hydrogels exhibit soft solid characteristics and demonstrate shorter contact times and diminished deformations upon impact with a solid surface. Moreover, in contrast to pure water droplets, the synergistic effect of elasticity and rapid water evaporation within hydrogel droplets gives rise to distinctive bouncing and trampolining dynamics on superheated surfaces [249].

Beyond conventional molecular liquids like water and ethanol, recent investigations have prioritized ionic liquids (ILs) for their emerging applications in thermal management and combustion mitigation [250]. Composed of asymmetric cation–anion pairs, ILs exhibit unique nonmolecular characteristics leading to thermal decomposition pathways distinct from molecular counterparts. Their impact dynamics reveal marked deviations from Newtonian fluids, particularly in the manifestation of the dynamic Leidenfrost effect, as visualized in Fig. 20 (g). In parallel, molten liquid metal (LM) droplets have emerged as transformative candidates in next-generation microelectronics fabrication, owing to their unique role in advanced deposition processes. Surface temperature [251] and functionalization critically influence LM droplet behavior, with gallium-based alloys presenting a notable case study. Upon airborne exposure, these alloys rapidly develop a viscoelastic oxide layer exhibiting pronounced adhesive characteristics [252]. Pre-impact droplet morphometry analyses, as shown in Fig. 20 (h), reveal non-spherical geometries with apical tail formations. Quantitatively, the oxide layer reduces the restitution coefficient by 45 % while increasing contact time by 36 %, collectively enhancing interfacial heat transfer efficiency. Mechanistically, oxidation-induced contact line modifications produce a distinctive scaling relationship where the maximum spread parameter correlates with the Weber number through a 1/2 power law [196], highlighting the coupled effects of surface chemistry and fluid physics in metallic droplet dynamics.

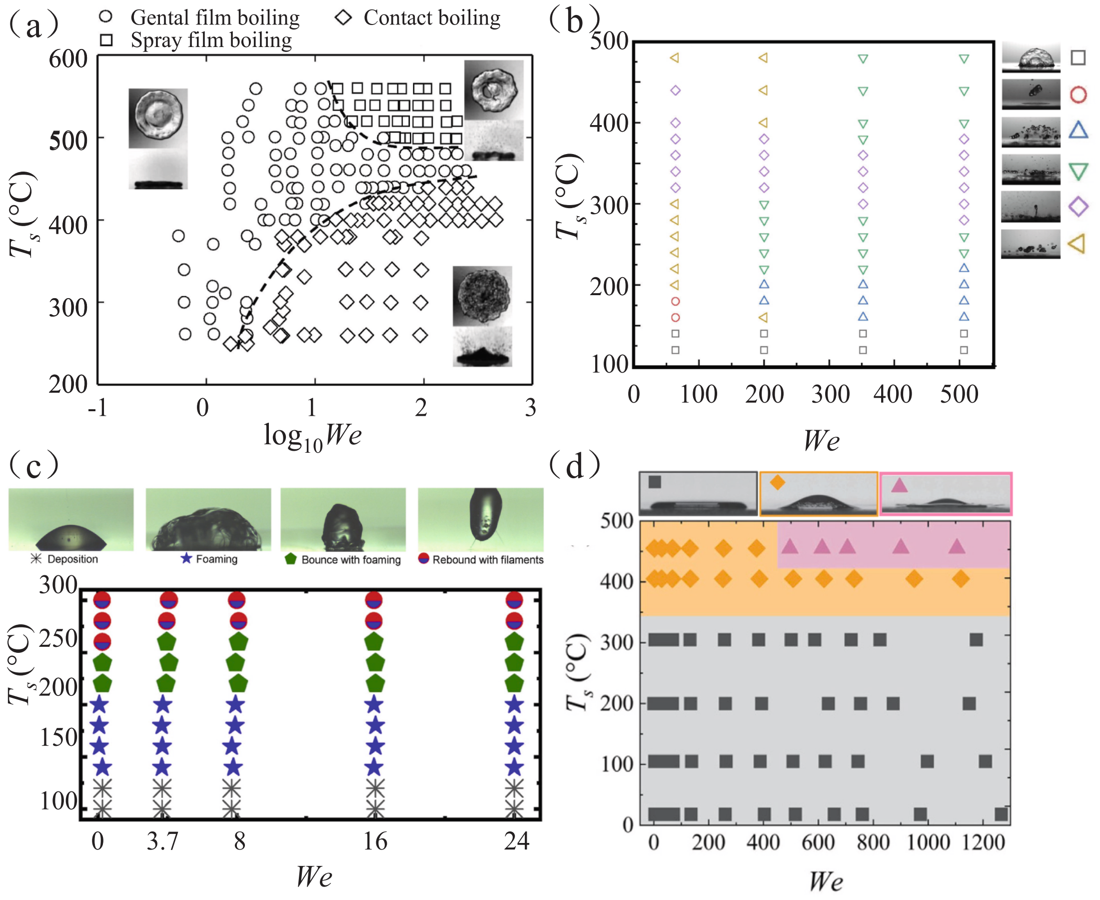

Fig. 21. Regime diagrams of different drops impinging on hydrophilic heated surfaces. (a) Water and FC-72 droplets [31]; (b) NaCl aqueous solution droplets [36]; (c) Viscoelastic (aqueous polyethylene oxide) droplet [179]; (d) Ionic liquid ([EMIM][SCN]) droplets [194].

5.2. Boiling regimes of complex fluid droplets

Significant research efforts have focused on characterizing boiling regimes during droplet impact on heated surfaces to elucidate transition mechanisms across diverse fluid systems. Building on foundational studies, Tran et al. [188] delineated the Weber number-temperature phase spaces for water and FC-72 droplets, identifying a tripartite regime classification: contact, gentle-film, and spraying-film boiling regimes (Fig. 21(a)). For NaCl aqueous solutions, salt crystal deposition elevates both boiling and Leidenfrost temperatures, resulting in six defined regimes (Fig. 21(b)) [36]. Notably, central jetting emerges at 280 °C–440 °C due to violent boiling-induced flow blockage during early spreading, with non-linear regime boundaries observed. Prasad et al. [253] demonstrate the effectiveness of surfactants in elevating the Leidenfrost temperature during droplet impact, showing that the Leidenfrost temperature increases with rising surfactant concentration. Likewise, nanoparticles have been found to significantly enhance the Leidenfrost temperature through the dispersion of nanobubbles [254]. The boiling regimes of nano-colloidal droplets can be categorized into five distinct types: contact boiling, spray boiling, rebounding Leidenfrost, residue rebounding Leidenfrost, and fragmenting Leidenfrost [255]. Polymer additives introduce further complexity, as demonstrated by microcellular foaming and viscoelastic filament formation under high molecular weight and concentration conditions (Fig. 21(c)) [179]. This behavior necessitates a novel regime classification distinct from Newtonian fluids. Ionic liquids, such as [EMIM][SCN], exhibit unique dynamics: the dynamic Leidenfrost effect is absent during glass impact due to insufficient vapor pressure from evaporation and thermal decomposition (Fig. 21(d)) [194].

Liquid metal (LM) droplets introduce additional challenges, with oxidation-driven viscosity changes significantly altering impact behavior. For gallium-based LMs, oxide film formation promotes splashing and secondary droplet ejection upon pool impact, with temperature-dependent intensification linked to oxidative effects [256]. Strikingly, in our culture, no studies to date have reported boiling regimes for LM droplets on heated solids, owing to their extreme boiling points (∼1300 °C) [196]. While Zhao et al. [257] comprehensively reviewed room-temperature LM impact dynamics, critical knowledge gaps persist regarding supercooled LM interactions with isothermal/non-isothermal surfaces—a frontier with implications for 3D printing, thermal interface materials [251], and spray coatings. Substrate properties and temperature minimally influence spreading factors but critically determine solidification outcomes due to LM low melting points (e.g., −19 °C) [251].

6. Current status, challenges, and future perspectives

This review offers a systematic analysis of the recent progress in interfacial dynamics and thermal transport mechanisms governing droplet-surface interactions. The current status is summarized below:

(1) Through synergistic integration of ultrahigh-speed photonic diagnostics with phase-contrast X-ray tomography, contemporary research has revolutionized our observational capabilities, providing unprecedented insights into previously inaccessible features such as the motion of daughter droplets within the bubble, vortex rings, and singular jet dynamics. Advanced PIV methodologies have the potential to provide insights into the three-dimensional nature of the transient fluid dynamics, and Infrared imaging captures the full-field thermal response with high spatial and temporal resolution. The advancement of emerging numerical models enables us to gain a deeper understanding of complex droplet-surface interaction phenomena. Commercial simulation software presents robust pre-built models and user-friendly interfaces. In contrast, open-source platforms offer enhanced flexibility, enabling researchers to implement customized physics and explore cutting-edge or emerging phenomena. These tools are well-suited for droplet impact research and the exploration of novel or intricate multiphase flow scenarios.

(2) The post-impact behavior of droplets on non-thermal substrates is governed by the competitive interplay of inertial, capillary, and viscous forces, with splashing dynamics being particularly sensitive to substrate topography and fluid properties. In contrast to non-thermal scenarios, heated surfaces introduce thermocapillary-driven phase transitions where surface temperature emerges as critical governing parameters, dictating boiling mode transitions through Leidenfrost temperature modulation, altering spreading kinematics and splashing criteria via vapor-mediated effects. The engineering applications encompass two domains: by engineering surfaces with custom-designed topography, precise manipulation of the Leidenfrost temperature shift can be accomplished, providing high heat flux spray cooling; the other is to promote droplet rebound through superhydrophobicity while enhancing energy conversion. The properties of the droplet have a considerable influence on droplet spreading and recoiling, thereby leading to a modification of the final boiling regime after impact. The increasing interest in non-Newtonian fluids, such as aqueous polymer solution, ionic liquids, and liquid metals, is ascribed to their distinctive properties, which possess considerable potential for potential cooling and combustion applications.

Droplet-surface thermal dynamics are determined by fluid-substrate interfacial synergies that govern phase-change phenomena [258], However, persistent knowledge gaps and technical challenges in this domain necessitate further investigation. Key challenges and future research directions include:

(1) Advances in surface engineering demand scalable production integrating durability and economy, which presents a considerable challenge. For instance, micro/nanotextured low-energy coatings reduce solid–liquid adhesion, yet their susceptibility to stress hinders industrial adoption [259]. Armored superhydrophobic designs exhibit unprecedented wear resistance (>1,000 cycles) [237], bridging the gap between lab-scale innovation and industrial applications.

(2) Emerging thermal management exploits complex fluids: The behavior of two-component mixed solution droplets on heated surfaces has emerged as a subject of significant interest in recent times. This research area has led to the discovery of hitherto unobserved yet crucial outcomes, as reported in reference [40]. Going forward, a quantitative investigation will be the central focus of future studies; Ionic liquids (ILs) uniquely suppress dynamic Leidenfrost effects, allowing precise droplet control for extreme cooling. Liquid metals enable ultrahigh heat flux dissipation but require fundamental studies on non-boiling impact dynamics (owing to extremely high boiling points) while addressing oxidation-induced mobility degradation [260] and metal corrosion.

(3) Simultaneously, dielectric spray cooling outperforms conventional cold plates in data centers, providing enhanced thermal uniformity through direct droplet-surface contact [261]. Critical future research priorities include the optimization of micro/nanostructures for phase-change intensification and the assessment of dielectric coolant-solid material compatibility for practical application.

Declaration of competing interest

The authors declare that they have no known competing financial interests or personal relationships that could have appeared to influence the work reported in this paper.

Acknowledgements

This study was financially supported by the National Natural Science Foundation of China (Nos. 52425601, 52327809, 82361138571), National Key Research and Development Program of China (No. 2023YFB4404104), and Beijing Natural Science Foundation (No. L233022). S.L. acknowledges the National Natural Science Foundation of China (Grant No. 12402306).

Data availability

Data will be made available on request.

References

[1] B. Li, S. Lin, Y. Wang, Q. Yuan, S.W. Joo, L. Chen, Promoting rebound of impinging viscoelastic droplets on heated superhydrophobic surfaces, New J. Phys. 22 (2020) 123001.

[2] A.A. Fyall, R.B. King, R.N.C. Strain, Rain erosion aspects of aircraft and guided missiles, Aeronaut. J. 66 (1962) 447–453.

[3] D. Lohse, Fundamental fluid dynamics challenges in inkjet printing, Annu. Rev. Fluid Mech. 54 (2022) 349–382.

[4] K.M. Wisdom, J.A. Watson, X. Qu, F. Liu, G.S. Watson, C.-H. Chen, Self-cleaning of superhydrophobic surfaces by self-propelled jumping condensate, Proc. Natl. Acad. Sci. U.S.A. 110 (2013) 7992–7997.

[5] L.E. Murr, W.L. Johnson, 3D metal droplet printing development and advanced materials additive manufacturing, J. Mater. Res. Technol. 6 (2017) 77–89.

[6] R.-N. Xu, L. Cao, G.-Y. Wang, J.-N. Chen, P.-X. Jiang, Experimental investigation of closed loop spray cooling with micro- and hybrid micro-/nano-engineered surfaces, Appl. Therm. Eng. 180 (2020) 115697.

[7] J. Kim, Spray cooling heat transfer: the state of the art, Int. J. Heat Fluid Fl. 28 (2007) 753–767.

[8] A. Habibi Khalaj, S.K. Halgamuge, A review on efficient thermal management of air- and liquid-cooled data centers: from chip to the cooling system, Appl. Energ. 205 (2017) 1165–1188.

[9] B. Li, C. Byon, Investigation of natural convection heat transfer around a radial heat sink with a concentric ring, Int. J. Heat Mass Tran. 89 (2015) 159–164.

[10] B. Li, Y.-J. Baik, C. Byon, Enhanced natural convection heat transfer of a chimney-based radial heat sink, Energ. Convers. Manage. 108 (2016) 422–428.

[11] A. Moradikazerouni, M. Afrand, J. Alsarraf, S. Wongwises, A. Asadi, T.K. Nguyen, Investigation of a computer CPU heat sink under laminar forced convection using a structural stability method, Int. J. Heat Mass Tran. 134 (2019) 1218–1226.

[12] F. Pourfattah, M. Sabzpooshani, Thermal management of a power electronic module employing a novel multi-micro nozzle liquid-based cooling system: a numerical study, Int. J. Heat Mass Tran. 147 (2020) 118928.

[13] Z.-Q. Yu, M.-T. Li, B.-Y. Cao, A comprehensive review on microchannel heat sinks for electronics cooling, Int. J. Extreme Manuf. 6 (2024) 022005.

[14] N. Xie, H. Xuegong, D. Tang, Visualization of microbubble dynamics behavior in rectangular capillary microgrooves under spray cooling condition, Heat Transfer Eng. 32 (2011) 1019–1025.

[15] D.P. Rini, R.-H. Chen, L.C. Chow, Bubble behavior and nucleate boiling heat transfer in saturated FC-72 spray cooling, J. Heat Transf. 124 (2001) 63–72.

[16] J. Breitenbach, I.V. Roisman, C. Tropea, From drop impact physics to spray cooling models: a critical review, Exp. Fluids 59 (2018) 55.

[17] S. Lin, B. Zhao, S. Zou, J. Guo, Z. Wei, L. Chen, Impact of viscous droplets on different wettable surfaces: Impact phenomena, the maximum spreading factor, spreading time and post-impact oscillation, J. Colloid Interf. Sci. 516 (2018) 86–97.

[18] M.R. Deendarlianto, T.P. Pradecta, W.H. Indarto, A.W. Mitrakusuma, Contact angle dynamics during the impact of single water droplet onto a hot flat practical stainless steel surface under medium Weber numbers, Heat Mass Transfer 57 (2021) 1097–1106.

[19] S.T. Thoroddsen, T.G. Etoh, K. Takehara, High-speed imaging of drops and bubbles, Annu. Rev. Fluid Mech. 40 (2008) 257–285.

[20] M. Shirota, M.A.J. van Limbeek, C. Sun, A. Prosperetti, D. Lohse, Dynamic Leidenfrost effect: relevant time and length scales, Phys. Rev. Lett. 116 (2016) 064501.

[21] M. Pasandideh-Fard, Y.M. Qiao, S. Chandra, J. Mostaghimi, Capillary effects during droplet impact on a solid surface, Phys. Fluids 8 (1996) 650–659.

[22] M. Bussmann, J. Mostaghimi, S. Chandra, On a three-dimensional volume tracking model of droplet impact, Phys. Fluids 11 (1999) 1406–1417.

[23] I. Yoon, S. Shin, Direct numerical simulation of droplet collision with stationary spherical particle: a comprehensive map of outcomes, Int. J. Multiphas. Flow 135 (2021) 103503.

[24] Y. Ge, L.S. Fan, 3-D modeling of the dynamics and heat transfer characteristics of subcooled droplet impact on a surface with film boiling, Int. J. Heat Mass Tran. 49 (2006) 4231–4249.

[25] P. Foltyn, D. Ribeiro, A. Silva, G. Lamanna, B. Weigand, Influence of wetting behavior on the morphology of droplet impacts onto dry smooth surfaces, Phys. Fluids 33 (2021).

[26] S. Chandra, C.T. Avedisian, On the collision of a droplet with a solid surface, P. Roy. Soc. A-Math. Phy. 432 (1991) 13–41.

[27] B. Gorin, G. Di Mauro, D. Bonn, H. Kellay, Universal aspects of droplet spreading dynamics in Newtonian and Non-Newtonian fluids, Langmuir 38 (2022) 2608–2613.

[28] D. Richard, C. Clanet, D. Quéré, Contact time of a bouncing drop, Nature 417 (2002) 811.

[29] W. Qi, P.B. Weisensee, Dynamic wetting and heat transfer during droplet impact on bi-phobic wettability-patterned surfaces, Phys. Fluids 32 (2020).

[30] P.B. Weisensee, J. Tian, N. Miljkovic, W.P. King, Water droplet impact on elastic superhydrophobic surfaces, Sci. Rep. 6 (2016) 30328.

[31] G. Liang, I. Mudawar, Review of drop impact on heated walls, Int. J. Heat Mass Tran. 106 (2017) 103–126.

[32] S. Ogata, R. Nakanishi, Effect of surface textures and wettability on droplet impact on a heated surface, Processes 9 (2021) 350.

[33] G. Mialhe, S. Tanguy, L. Tranier, E.-R. Popescu, D. Legendre, An extended model for the direct numerical simulation of droplet evaporation. Influence of the Marangoni convection on Leidenfrost droplet, J. Comput. Phys. 491 (2023) 112366.

[34] Y. Liu, Y. Zheng, Y. Zhou, W. Zhao, Y. Li, S. Tang, C. Wang, S. Wang, Y. Chai, P. Zhu, Self-lubricated bouncing of hot droplets, Newton 1 (2025).

[35] L. Liu, G. Cai, P.A. Tsai, Drop impact on heated nanostructures, Langmuir 36 (2020) 10051–10060.

[36] J. Zhu, X. Chen, J. Sheng, S. Li, T. Lu, X. Chen, Hydrodynamics and crystallization of NaCl aqueous solution droplet impact on heated surface, Appl. Therm. Eng. 219 (2023) 119670.

[37] J. Wang, Y. Wu, Y. Cao, G. Li, Y. Liao, Influence of surface roughness on contact angle hysteresis and spreading work, Colloid Polym. Sci. 298 (2020) 1107–1112.

[38] C. Liu, J. Hu, G. Zhen, J. Chen, H. Chen, S. Huang, Y. Liu, Droplet interactions with hot surfaces: boiling modes, Leidenfrost temperature, dynamics, and applications, Small (2025) 2501592.

[39] R. Hatakenaka, J. Breitenbach, I.V. Roisman, C. Tropea, Y. Tagawa, Magic carpet breakup of a drop impacting onto a heated surface in a depressurized environment, Int. J. Heat Mass Tran. 145 (2019) 118729.

[40] Z. Tang, T. Yu, Z. Ke, B. Lai, Y. Gao, Y. Zhang, Experimental investigation on boiling regime transformation when the binary-droplet impact on the superheated surface, Appl. Therm. Eng. 233 (2023) 121194.

[41] B.T. Ng, Y.M. Hung, M.K. Tan, Suppression of the Leidenfrost effect via low frequency vibrations, Soft Matter 11 (2015) 775–784.

[42] O. Ozkan, A. Shahriari, V. Bahadur, Electrostatic suppression of the Leidenfrost state using AC electric fields, Appl. Phys. Lett. 111 (2017) 141608.

[43] C. Josserand, S.T. Thoroddsen, Drop impact on a solid surface, Annu. Rev. Fluid Mech. 48 (2016) 365–391.

[44] D.A. Burzynski, I.V. Roisman, S.E. Bansmer, On the splashing of high-speed drops impacting a dry surface, J. Fluid Mech. 892 (2020) A2.

[45] C. Clanet, J.C. Lasheras, Transition from dripping to jetting, J. Fluid Mech. 383 (1999) 307–326.

[46] N. Blanken, M.S. Saleem, C. Antonini, M.-J. Thoraval, Rebound of self-lubricating compound drops, Sci. Adv. 6 (2020) eaay3499.

[47] Y. Wang, Y. Zhao, L. Sun, A.A. Mehrizi, S. Lin, J. Guo, L. Chen, Successive rebounds of impinging water droplets on superhydrophobic surfaces, Langmuir 38 (2022) 3860–3867.

[48] C.W. Visser, Y. Tagawa, C. Sun, D. Lohse, Microdroplet impact at very high velocity, Soft Matter 8 (2012) 10732–10737.

[49] M. Versluis, High-speed imaging in fluids, Exp. Fluids 54 (2013) 1458.

[50] P.R. Gunjal, V.V. Ranade, R.V. Chaudhari, Dynamics of drop impact on solid surface: experiments and VOF simulations, AIChE J 51 (2005) 59–78.

[51] J.B. Lee, D. Derome, A. Dolatabadi, J. Carmeliet, Energy budget of liquid drop impact at maximum spreading: numerical simulations and experiments, Langmuir 32 (2016) 1279–1288.

[52] E.Q. Li, K.R. Langley, Y.S. Tian, P.D. Hicks, S.T. Thoroddsen, Double contact during drop impact on a solid under reduced air pressure, Phys. Rev. Lett. 119 (2017) 214502.

[53] E.Q. Li, S.T. Thoroddsen, Time-resolved imaging of a compressible air disc under a drop impacting on a solid surface, J. Fluid Mech. 780 (2015) 636–648.

[54] S. Lin, D. Wang, L. Zhang, Y. Jin, Z. Li, E. Bonaccurso, Z. You, X. Deng, L. Chen, Macrodrop-impact-mediated fluid microdispensing, Adv. Sci. 8 (2021) 2101331.

[55] M.V. Gielen, P. Sleutel, J. Benschop, M. Riepen, V. Voronina, C.W. Visser, D. Lohse, J.H. Snoeijer, M. Versluis, H. Gelderblom, Oblique drop impact onto a deep liquid pool, Phys. Rev. Fluids 2 (2017) 083602.

[56] S.K. Alghoul, C.N. Eastwick, D.B. Hann, Normal droplet impact on horizontal moving films: an investigation of impact behaviour and regimes, Exp. Fluids 50 (2011) 1305–1316.

[57] C.W. Visser, P.E. Frommhold, S. Wildeman, R. Mettin, D. Lohse, C. Sun, Dynamics of high-speed micro-drop impact: numerical simulations and experiments at frame-to-frame times below 100 ns, Soft Matter 11 (2015) 1708–1722.

[58] W. Zhao, S. Lin, L. Chen, E.Q. Li, S.T. Thoroddsen, M.-J. Thoraval, Jetting from an impacting drop containing a particle, Phys. Fluids 32 (2020).

[59] L. Chen, E. Bonaccurso, P. Deng, H. Zhang, Droplet impact on soft viscoelastic surfaces, Phys. Rev. E 94 (2016).

[60] L. Chen, L. Li, Z. Li, K. Zhang, Submillimeter-sized bubble entrapment and a high-speed jet emission during droplet impact on solid surfaces, Langmuir 33 (2017) 7225–7230.

[61] J.R. Castrejón-Pita, R. Castrejón-García, I.M. Hutchings, High speed shadowgraphy for the study of liquid drops, in: J. Klapp, A. Medina, A. Cros, C. A. Vargas (Eds.), Fluid Dynamics in Physics, Engineering and Environmental Applications, Springer, Berlin Heidelberg, Berlin, Heidelberg, 2013, pp. 121–137.

[62] S. Kim, Z. Wu, E. Esmaili, J. Dombroskie, S. Jung, How a raindrop gets shattered on biological surfaces, Proc. Natl. Acad. Sci. U.S.A. 117 (2020) 202002924.

[63] M. Piskunov, J. Breitenbach, J. Schmidt, P. Strizhak, C. Tropea, I. Roisman, Secondary atomization of water-in-oil emulsion drops impinging on a heated surface in the film boiling regime, Int. J. Heat Mass Tran. 165 (2021) 120672.

[64] S.T. Thoroddsen, K. Takehara, T.G. Etoh, Bubble entrapment through topological change, Phys. Fluids 22 (2010).

[65] M.M. Driscoll, S.R. Nagel, Ultrafast interference imaging of air in splashing dynamics, Phys. Rev. Lett. 107 (2011) 154502.

[66] R. Kaviani, J.M. Kolinski, High resolution interferometric imaging of liquid-solid interfaces with HOTNNET, Exp. Mech. 63 (2023) 309–321.

[67] M.M. Driscoll, C.S. Stevens, S.R. Nagel, Thin film formation during splashing of viscous liquids, Phys. Rev. E 82 (2010) 036302.

[68] S.W. Wilkins, T.E. Gureyev, D. Gao, A. Pogany, A.W. Stevenson, Phase-contrast imaging using polychromatic hard X-rays, Nature 384 (1996) 335–338.

[69] J. Lee, B.M. Weon, J. Je, X-ray phase-contrast imaging of dynamics of complex fluids, J. Phys. D Appl. Phys. 46 (2013) 4006.

[70] G. Agbaglah, M.J. Thoraval, S.T. Thoroddsen, L.V. Zhang, K. Fezzaa, R.D. Deegan, Drop impact into a deep pool: vortex shedding and jet formation, J. Fluid Mech. 764 (2015) R1.

[71] J. Lee, S. Park, J. Lee, B.M. Weon, K. Fezzaa, J. Je, Origin and dynamics of vortex rings in drop splashing, Nat. Commun. 6 (2015) 8187.

[72] J.S. Lee, B.M. Weon, J.H. Je, K. Fezzaa, How does an air film evolve into a bubble during drop impact? Phys. Rev. Lett. 109 (2012) 204501.

[73] J.S. Lee, B.M. Weon, S.J. Park, J.T. Kim, J. Pyo, K. Fezzaa, J.H. Je, Air evolution during drop impact on liquid pool, Sci. Rep. 10 (2020) 5790.

[74] S.T. Thoroddsen, T.G. Etoh, K. Takehara, N. Ootsuka, Y. Hatsuki, The air bubble entrapped under a drop impacting on a solid surface, J. Fluid Mech. 545 (2005) 203–212.

[75] N. Saneie, V. Kulkarni, B. Treska, K. Fezzaa, N. Patankar, S. Anand, Microbubble dynamics and heat transfer in boiling droplets, Int. J. Heat Mass Tran. 176 (2021) 121413.

[76] L.V. Zhang, J. Toole, K. Fezzaa, R.D. Deegan, Evolution of the ejecta sheet from the impact of a drop with a deep pool, J. Fluid Mech. 690 (2011) 5–15.

[77] M.J. Thoraval, K. Takehara, T.G. Etoh, S.T. Thoroddsen, Drop impact entrapment of bubble rings, J. Fluid Mech. 724 (2013) 234–258.

[78] A. Gultekin, N. Erkan, U. Colak, S. Suzuki, PIV measurement inside single and double droplet interaction on a solid surface, Exp. Fluids 61 (2020) 218.

[79] R.J. Adrian, Twenty years of particle image velocimetry, Exp. Fluids 39 (2005) 159–169.

[80] M.I. Smith, V. Bertola, Particle velocimetry inside Newtonian and non-Newtonian droplets impacting a hydrophobic surface, Exp. Fluids 50 (2011) 1385–1391.

[81] S.S. Kumar, A. Karn, R.E.A. Arndt, J. Hong, Internal flow measurements of drop impacting a solid surface, Exp. Fluids 58 (2017) 12.

[82] A. Bouillant, T. Mouterde, P. Bourrianne, A. Lagarde, C. Clanet, D. Quéré, Leidenfrost wheels, Nat. Phys. 14 (2018) 1188–1192.

[83] A. Melling, Tracer particles and seeding for particle image velocimetry, Meas. Sci. Technol. 8 (1997) 1406.

[84] S. Scharnowski, C.J. Kähler, Particle image velocimetry - Classical operating rules from today's perspective, Opt. Lasers Eng. 135 (2020) 106185.

[85] S. Schubert, J. Steigerwald, A.K. Geppert, B. Weigand, G. Lamanna, Micro-PIV study on the influence of viscosity on the dynamics of droplet impact onto a thin film, Exp. Fluids 65 (2024) 69.

[86] C.J.M. van Rijn, J. Westerweel, B. van Brummen, A. Antkowiak, D. Bonn, Self-similar jet evolution after drop impact on a liquid surface, Phys. Rev. Fluids 6 (2021) 034801.

[87] N. Erkan, K. Okamoto, Full-field spreading velocity measurement inside droplets impinging on a dry solid surface, Exp. Fluids 55 (2014) 1845.

[88] I.V. Roisman, R. Rioboo, C. Tropea, Normal impact of a liquid drop on a dry surface: model for spreading and receding, Proc. R. Soc. Lond. A 458 (2002) 1411–1430.

[89] A.L. Yarin, D.A. Weiss, Impact of drops on solid surfaces: self-similar capillary waves, and splashing as a new type of kinematic discontinuity, J. Fluid Mech. 283 (2006) 141–173.

[90] I.V. Roisman, E. Berberović, C. Tropea, Inertia dominated drop collisions. I. On the universal flow in the lamella, Phys. Fluids 21 (2009).

[91] N. Erkan, Full-field spreading velocity measurement inside droplets impinging on a dry solid-heated surface, Exp. Fluids 60 (2019) 88.

[92] S.T. Thoroddsen, The ejecta sheet generated by the impact of a drop, J. Fluid Mech. 451 (2002) 373–381.

[93] N. Takagaki, S. Komori, Air–water mass transfer mechanism due to the impingement of a single liquid drop on the air–water interface, Int. J. Multiphas. Flow 60 (2014) 30–39.

[94] H. Toshio, S. Jun, High-speed scanning stereoscopic PIV for 3D vorticity measurement in liquids, Meas. Sci. Technol. 15 (2004) 1067.

[95] H. Kinoshita, S. Kaneda, T. Fujii, M. Oshima, Three-dimensional measurement and visualization of internal flow of a moving droplet using confocal micro-PIV, Lab Chip 7 (2007) 338–346.

[96] M. Kunihide, M. Itaru, The behavior of a water droplet on heated surfaces, Int. J. Heat Mass Tran. 27 (1984) 781–791.

[97] J.M. Ingram, A.F. Averill, P.G. Holborn, P. Battersby, C.M. Benson, Surface temperature generation during drop weight mechanical impact and the usefulness of dynamic thermocouple measurements for predicting impact ignition of flammable gases, J. Loss Prevent. Proc. 55 (2018) 10–18.

[98] L. Liu, Y. Zhang, G. Cai, P.A. Tsai, High-speed dynamics and temperature variation during drop impact on a heated surface, Int. J. Heat Mass Tran. 189 (2022) 122710.

[99] D. Chatzikyriakou, S.P. Walker, C.P. Hale, G.F. Hewitt, The measurement of heat transfer from hot surfaces to non-wetting droplets, Int. J. Heat Mass Tran. 54 (2011) 1432–1440.

[100] H. Li, I.V. Roisman, C. Tropea, Influence of solidification on the impact of supercooled water drops onto cold surfaces, Exp. Fluids 56 (2015) 133.

[101] J. Li, P. Weisensee, Droplet impact and Leidenfrost dynamics on a heated post, Int. J. Heat Mass Tran. 201 (2023) 123581.

[102] S. Bagavathiappan, B.B. Lahiri, T. Saravanan, J. Philip, T. Jayakumar, Infrared thermography for condition monitoring – a review, Infrared Phys. Techn. 60 (2013) 35–55.

[103] L. Reggiani, E. Alfinito, Revisiting the Boltzmann Derivation of the Stefan Law, Fluct. Noise Lett. 21 (2022) 2230001.

[104] W.L. Wolfe, G.J. Zissis, The Infrared Handbook, Office of Naval Research, Department of the Navy, Arlington, 1978.

[105] G.M. Hale, M.R. Querry, Optical constants of water in the 200-nm to 200-microm wavelength region, Appl. Opt. 12 (1973) 555–563.

[106] A. Gholijani, C. Schlawitschek, T. Gambaryan-Roisman, P. Stephan, Heat transfer during drop impingement onto a hot wall: the influence of wall superheat, impact velocity, and drop diameter, Int. J. Heat Mass Tran. 153 (2020) 119661.

[107] J. Jung, S. Jeong, H. Kim, Investigation of single-droplet/wall collision heat transfer characteristics using infrared thermometry, Int. J. Heat Mass Tran. 92 (2016) 774–783.

[108] V. Talari, P. Behar, Y. Lu, E. Haryadi, D. Liu, Leidenfrost drops on micro/nanostructured surfaces, Front. Energy 12 (2018) 22–42.

[109] M. Jiang, Y. Wang, F. Liu, H. Du, Y. Li, H. Zhang, S. To, S. Wang, C. Pan, J. Yu, D. Quéré, Z. Wang, Inhibiting the Leidenfrost effect above 1,000 °C for sustained thermal cooling, Nature 601 (2022) 568–572.

[110] Z. Jian, C. Josserand, S. Popinet, P. Ray, S. Zaleski, Two mechanisms of droplet splashing on a solid substrate, J. Fluid Mech. 835 (2017) 1065–1086.

[111] S. Popinet, Numerical models of surface tension, Annu. Rev. Fluid Mech. 50 (2018) 49–75.

[112] S. Osher, J.A. Sethian, Fronts propagating with curvature-dependent speed: Algorithms based on Hamilton-Jacobi formulations, J. Comput. Phys. 79 (1988) 12–49.

[113] S. Osher, R.P. Fedkiw, Level set methods: an overview and some recent results, J. Comput. Phys. 169 (2001) 463–502.

[114] C.W. Hirt, B.D. Nichols, Volume of fluid (VOF) method for the dynamics of free boundaries, J. Comput. Phys. 39 (1981) 201–225.

[115] A. Karma, W.-J. Rappel, Phase-field method for computationally efficient modeling of solidification with arbitrary interface kinetics, Phys. Rev. E 53 (1996) R3017–R3020.

[116] S. Chen, G.D. Doolen, Lattice boltzmannn method for fluid flows, Annu. Rev. Fluid Mech. 30 (1998) 329–364.

[117] J.A. Sethian, P. Smereka, Level set methods for fluid interfaces, Annu. Rev. Fluid Mech. 35 (2003) 341–372.

[118] S.H. Lee, N. Hur, S. Kang, A numerical analysis of drop impact on liquid film by using a level set method, J. Mech. Sci. Technol. 25 (2011) 2567–2572.

[119] G. Son, N. Hur, A level set formulation for incompressible two-phase flows on nonorthogonal grids, Numer. Heat Tr. b: Fund. 48 (2005) 303–316.

[120] S. Lin, Y. Wang, L. Sun, A.A. Mehrizi, Y. Jin, L. Chen, Experimental and numerical investigations on the spreading dynamics of impinging liquid droplets on diverse wettable surfaces, Int. J. Multiphas. Flow 153 (2022) 104135.

[121] Q. Tang, S. Xiang, S. Lin, Y. Jin, C. Antonini, L. Chen, Enhancing droplet rebound on superhydrophobic cones, Phys. Fluids 35 (2023).

[122] E. Olsson, G. Kreiss, A conservative level set method for two phase flow, J. Comput. Phys. 210 (2005) 225–246.

[123] S.P. van der Pijl, A. Segal, C. Vuik, P. Wesseling, A mass-conserving Level-Set method for modelling of multi-phase flows, Int. J. Numer. Meth. Fl. 47 (2005) 339–361.

[124] F. Losasso, R. Fedkiw, S. Osher, Spatially adaptive techniques for level set methods and incompressible flow, Comput. Fluids 35 (2006) 995–1010.

[125] X. Gu, L. Chen, F. Wang, Y. Wang, Y. Li, W. Wu, M. Hu, D. Deng, Numerical simulation of droplet impacting on a microstructured surface: geometry, wettability, and control of jump-off force, Phys. Fluids 36 (2024) 022025.

[126] S.F. Lunkad, V.V. Buwa, K.D.P. Nigam, Numerical simulations of drop impact and spreading on horizontal and inclined surfaces, Chem. Eng. Sci. 62 (2007) 7214–7224.

[127] W.J. Rider, D.B. Kothe, Reconstructing volume tracking, J. Comput. Phys. 141 (1998) 112–152.

[128] V. Boniou, T. Schmitt, A. Vié, Comparison of interface capturing methods for the simulation of two-phase flow in a unified low-Mach framework, Int. J. Multiphas. Flow 149 (2022) 103957.

[129] L. Xia, F. Chen, T. Liu, D. Zhang, Y. Tian, D. Zhang, Phase-field simulations of droplet impact on superhydrophobic surfaces, Int. J. Mech. Sci. 240 (2023) 107957.

[130] Q. Zhang, T.-Z. Qian, X.-P. Wang, Phase field simulation of a droplet impacting a solid surface, Phys. Fluids 28 (2016).

[131] M. Shen, B.Q. Li, Q. Yang, Y. Bai, Y. Wang, S. Zhu, B. Zhao, T. Li, Y. Hu, A modified phase-field three-dimensional model for droplet impact with solidification, Int. J. Multiphas. Flow 116 (2019) 51–66.

[132] H. Xu, J. Wang, H. Wang, B. Li, K. Yu, J. Yao, W. Zhang, L. Zuo, Numerical investigation of droplet impact and heat transfer on hot substrates under an electric field, Int. J. Heat Mass Tran. 229 (2024) 125721.

[133] Z. Fu, H. Jin, G. Yao, D. Wen, Droplet impact simulation with Cahn–Hilliard phase field method coupling Navier-slip boundary and dynamic contact angle model, Phys. Fluids 36 (2024).

[134] N. Samkhaniani, A. Stroh, M. Holzinger, H. Marschall, B. Frohnapfel, M. Wörner, Bouncing drop impingement on heated hydrophobic surfaces, Int. J. Heat Mass Tran. 180 (2021) 121777.

[135] L.C. Malan, A.G. Malan, S. Zaleski, P.G. Rousseau, A geometric VOF method for interface resolved phase change and conservative thermal energy advection, J. Comput. Phys. 426 (2021) 109920.

[136] B.-L. Wei, J. Zhang, M.-J. Ni, A hybrid phase field - volume of fluid method for the simulation of three-dimensional binary solidification in the presence of gas bubble, J. Comput. Phys. 524 (2025) 113720.

[137] Z. Huang, G. Lin, A.M. Ardekani, A consistent and conservative Phase-Field model for thermo-gas-liquid-solid flows including liquid-solid phase change, J. Comput. Phys. 449 (2022) 110795.

[138] Z. Guo, J. Mi, S. Xiong, P.S. Grant, Phase field study of the tip operating state of a freely growing dendrite against convection using a novel parallel multigrid approach, J. Comput. Phys. 257 (2014) 278–297.

[139] J.J. Hoyt, M. Asta, A. Karma, Atomistic and continuum modeling of dendritic solidification, Mater. Sci. Eng.: r: Rep. 41 (2003) 121–163.

[140] S. Lyu, K. Wang, Z. Zhang, A. Pedrono, C. Sun, D. Legendre, A hybrid VOF-IBM method for the simulation of freezing liquid films and freezing drops, J. Comput. Phys. 432 (2021) 110160.

[141] A.G. Marín, O.R. Enríquez, P. Brunet, P. Colinet, J.H. Snoeijer, Universality of tip singularity formation in freezing water drops, Phys. Rev. Lett. 113 (2014) 054301.

[142] C. Wang, M.-C. Lai, Z. Zhang, An improved phase-field algorithm for simulating the impact of a drop on a substrate in the presence of surfactants, J. Comput. Phys. 499 (2024) 112722.

[143] R.G.M. van der Sman, S. van der Graaf, Diffuse interface model of surfactant adsorption onto flat and droplet interfaces, Rheol. Acta 46 (2006) 3–11.

[144] H. Abels, H. Garcke, G. GrÜN, Thermodynamically consistent, frame indifferent diffuse interface models for incompressible two-phase flows with different densities, Math. Models Methods Appl. Sci. 22 (2012) 1150013.

[145] S. Zhao, J. Zhang, M.-J. Ni, Boiling and evaporation model for liquid-gas flows: a sharp and conservative method based on the geometrical VOF approach, J. Comput. Phys. 452 (2022) 110908.

[146] E. Cipriano, A.E. Saufi, A. Frassoldati, T. Faravelli, S. Popinet, A. Cuoci, Multicomponent droplet evaporation in a geometric volume-of-fluid framework, J. Comput. Phys. 507 (2024) 112955.

[147] K. Bazesefidpar, L. Brandt, O. Tammisola, A dual resolution phase-field solver for wetting of viscoelastic droplets, Int. J. Numer. Meth. Fl. 94 (2022) 1517–1541.

[148] J. Guo, S. Lin, B. Zhao, X. Deng, L. Chen, Spreading of impinging droplets on nanostructured superhydrophobic surfaces, Appl. Phys. Lett. 113 (2018) 071602.

[149] H.-B. Nguyen, J.-C. Chen, A numerical study of thermocapillary migration of a small liquid droplet on a horizontal solid surface, Phys. Fluids 22 (2010) 062102.

[150] M. Piskunov, A. Piskunova, I. Vozhakov, S. Misyura, Numerical contact line behavior prediction for drop-wall impact using Basilisk, J. Phys. Conf. Ser. 2766 (2024) 012073.

[151] Y. Li, J. Cheng, Modeling liquid droplet impact on a micropillar-arrayed viscoelastic surface via mechanically averaged responses, Eng. Appl. Comput. Fluid Mech. 17 (2023) 2194949.

[152] J. Philippi, P.-Y. Lagrée, A. Antkowiak, Drop impact on a solid surface: short-time self-similarity, J. Fluid Mech. 795 (2016) 96–135.

[153] D.S.N. Abg Shamsuddin, A.F. Mohd Fekeri, A. Muchtar, F. Khan, B.C. Khor, B. H. Lim, M.I. Rosli, M.S. Takriff, Computational fluid dynamics modelling approaches of gas explosion in the chemical process industry: a review, Process Saf. Environ. 170 (2023) 112–138.

[154] H. Jasak, OpenFOAM: Open source CFD in research and industry, Int. J. Nav. Arch. Ocean 1 (2009) 89–94.

[155] M. Schremb, S. Borchert, E. Berberovic, S. Jakirlic, I.V. Roisman, C. Tropea, Computational modelling of flow and conjugate heat transfer of a drop impacting onto a cold wall, Int. J. Heat Mass Tran. 109 (2017) 971–980.

[156] S.L. Brunton, B.R. Noack, P. Koumoutsakos, Machine learning for fluid mechanics, Annu. Rev. Fluid Mech. 52 (2020) 477–508.

[157] A. Azimi Yancheshme, S. Hassantabar, K. Maghsoudi, S. Keshavarzi, R. Jafari, G. Momen, Integration of experimental analysis and machine learning to predict drop behavior on superhydrophobic surfaces, Chem. Eng. J. 417 (2021) 127898.

[158] A.K. Dickerson, M.E. Alam, J. Buckelew, N. Boyum, D. Turgut, Predictive modeling of drop impact force on concave targets, Phys. Fluids 34 (2022).

[159] E. Klaseboer, R. Manica, D.Y.C. Chan, Universal behavior of the initial stage of drop impact, Phys. Rev. Lett. 113 (2014) 194501.

[160] A.L. Yarin, Drop impact dynamics: splashing, spreading, receding, bouncing, Annu. Rev. Fluid Mech. 38 (2006) 159–192.

[161] R. Rioboo, C. Tropea, M. Marengo, Outcomes from a drop impact on solid surfaces, Atom. Spray 11 (2001) 12.

[162] L. Xu, W.W. Zhang, S.R. Nagel, Drop splashing on a dry smooth surface, Phys. Rev. Lett. 94 (2005) 184505.

[163] L. Xu, L. Barcos, S.R. Nagel, Splashing of liquids: Interplay of surface roughness with surrounding gas, Phys. Rev. E 76 (2007) 066311.

[164] H. Zhang, X. Zhang, X. Yi, F. He, F. Niu, P. Hao, Effect of wettability on droplet impact: spreading and splashing, Exp. Therm Fluid Sci. 124 (2021) 110369.

[165] H. Almohammadi, A. Amirfazli, Droplet impact: Viscosity and wettability effects on splashing, J. Colloid Interf. Sci. 553 (2019) 22–30.

[166] H. Zhang, X. Zhang, X. Yi, F. He, F. Niu, P. Hao, Reversed role of liquid viscosity on drop splash, Phys. Fluids 33 (2021) 052103.

[167] L. Yang, Z. Li, T. Yang, Y. Chi, P. Zhang, Experimental study on droplet splash and receding breakup on a smooth surface at atmospheric pressure, Langmuir 37 (2021) 10838–10848.

[168] T.C. de Goede, N. Laan, K.G. de Bruin, D. Bonn, Effect of wetting on drop splashing of Newtonian fluids and blood, Langmuir 34 (2018) 5163–5168.

[169] A. Latka, A.M.P. Boelens, S.R. Nagel, J.J. de Pablo, Drop splashing is independent of substrate wetting, Phys. Fluids 30 (2018).

[170] S. Lin, L. Zhou, B. Liu, Q. Xu, L. Chen, Z. Li, The roles of surface temperature and roughness in droplet splashing, Int. J. Heat Mass Tran. 220 (2024) 124959.

[171] I.V. Roisman, J. Breitenbach, C. Tropea, Thermal atomisation of a liquid drop after impact onto a hot substrate, J. Fluid Mech. 842 (2018) 87–101.

[172] H.J.J. Staat, T. Tran, B. Geerdink, G. Riboux, C. Sun, J.M. Gordillo, D. Lohse, Phase diagram for droplet impact on superheated surfaces, J. Fluid Mech. 779 (2015) R3.

[173] J.D. Bernardin, C.J. Stebbins, I. Mudawar, Mapping of impact and heat transfer regimes of water drops impinging on a polished surface, Int. J. Heat Mass Tran. 40 (1997) 247–267.

[174] J.D. Bernardin, I. Mudawar, Film boiling heat transfer of droplet streams and sprays, Int. J. Heat Mass Tran. 40 (1997) 2579–2593.

[175] J. Yang, Y. Li, D. Wang, Y. Fan, Y. Ma, F. Yu, J. Guo, L. Chen, Z. Wang, X. Deng, A standing Leidenfrost drop with sufi whirling, Proc. Natl. Acad. Sci. U.S.A. 120 (2023) e2305567120.

[176] H.Y. Erbil, Evaporation of pure liquid sessile and spherical suspended drops: a review, Adv. Colloid Interfac. 170 (2012) 67–86.

[177] P. Agrawal, G. Tomar, S. Dash, Reemergence of trampolining in a Leidenfrost droplet, Phys. Rev. Fluids 10 (2025) 053606.

[178] P. Agrawal, S. Dash, Droplet trampolining on heated surfaces in the transitional boiling regime, Int. J. Heat Mass Tran. 190 (2022) 122811.

[179] B. Li, L. Chen, S. Joo, Impact dynamics of Newtonian and viscoelastic droplets on heated surfaces at low Weber number, Case Stud. Therm. Eng. 26 (2021) 101109.

[180] A.-L. Biance, C. Clanet, D. Quéré, Leidenfrost drops, Phys. Fluids 15 (2003) 1632–1637.

[181] H.Y. Lo, Y. Liu, L. Xu, Mechanism of contact between a droplet and an atomically smooth substrate, Phys. Rev. X 7 (2017) 021036.

[182] J.C. Burton, A.L. Sharpe, R.C.A. van der Veen, A. Franco, S.R. Nagel, Geometry of the vapor layer under a leidenfrost drop, Phys. Rev. Lett. 109 (2012) 074301.

[183] T.A. Caswell, Dynamics of the vapor layer below a Leidenfrost drop, Phys. Rev. E 90 (2014) 013014.

[184] G.C. Lee, H. Noh, H.J. Kwak, T.K. Kim, H.S. Park, K. Fezzaa, M.H. Kim, Measurement of the vapor layer under a dynamic Leidenfrost drop, Int. J. Heat Mass Tran. 124 (2018) 1163–1171.

[185] P. Zhao, G.K. Hargrave, H.K. Versteeg, C.P. Garner, B.A. Reid, E.J. Long, H. Zhao, The dynamics of droplet impact on a heated porous surface, Chem. Eng. Sci. 190 (2018) 232–247.

[186] M. Khavari, C. Sun, D. Lohse, T. Tran, Fingering patterns during droplet impact on heated surfaces, Soft Matter 11 (2015) 3298–3303.

[187] T. Tran, H.J.J. Staat, A. Prosperetti, C. Sun, D. Lohse, Drop impact on superheated surfaces, Phys. Rev. Lett. 108 (2012) 036101.

[188] T. Tran, H.J.J. Staat, A. Susarrey-Arce, T.C. Foertsch, A. van Houselt, H.J.G. E. Gardeniers, A. Prosperetti, D. Lohse, C. Sun, Droplet impact on superheated micro-structured surfaces, Soft Matter 9 (2013) 3272–3282.

[189] H. Nair, H.J.J. Staat, T. Tran, A. van Houselt, A. Prosperetti, D. Lohse, C. Sun, The Leidenfrost temperature increase for impacting droplets on carbon-nanofiber surfaces, Soft Matter 10 (2014) 2102–2109.

[190] V. Bertola, An experimental study of bouncing Leidenfrost drops: comparison between Newtonian and viscoelastic liquids, Int. J. Heat Mass Tran. 52 (2009) 1786–1793.

[191] V. Bertola, Effect of polymer concentration on the dynamics of dilute polymer solution drops impacting on heated surfaces in the Leidenfrost regime, Exp. Therm Fluid Sci. 52 (2014) 259–269.

[192] B. Li, A.A. Mehrizi, S. Lin, S. Joo, L. Chen, Dynamic behaviors of impinging viscoelastic droplets on superhydrophobic surfaces heated above the boiling temperature, Int. J. Heat Mass Tran. 183 (2022) 122080.

[193] S.-Y. Chen, D.-Q. Zhu, H.-J. Xing, Q. Zhao, Z.-F. Zhou, B. Chen, Droplet formation and impingement dynamics of low-boiling refrigerant on solid surfaces with different roughness under atmospheric pressure, Appl. Sci. 12 (2022) 8549.

[194] L. Liu, B. He, W. Wang, G. Cai, P.A. Tsai, Ionic liquid drop impact onto heated surfaces, Phys. Rev. Fluids 8 (2023) 073602.

[195] W. Babatain, M.S. Kim, M.M. Hussain, From droplets to devices: recent advances in liquid metal droplet enabled electronics, Adv. Funct. Mater. 34 (2024) 2308116.

[196] R. McGuan, R.N. Candler, H.P. Kavehpour, Spreading and contact-line arrest dynamics of impacting oxidized liquid-metal droplets, Phys. Rev. Fluids 6 (2021) L111601.

[197] C. Li, J. Wang, L. Zheng, Z. Wang, Q. Liu, R. Yang, Experiment study on adhesion dynamic characteristics of droplet impacting on an inclined heated surface, Surf. Interfaces 51 (2024) 104602.

[198] A. Sreenivasan, S. Deivandren, Splashing of fuel drops impacting on heated solid surfaces, Phys. Fluids 32 (2020).

[199] G. Riboux, J.M. Gordillo, Experiments of drops impacting a smooth solid surface: a model of the critical impact speed for drop splashing, Phys. Rev. Lett. 113 (2014) 024507.

[200] R. Tao, C. Hao, B. Ji, F. Yu, X. Wang, J. Wang, P. Sun, Y. Jin, H. Gu, B. Li, S. Wang, Z. Wang, Surface nanostructures promote droplet splash on hot substrates, Nano Lett. 24 (2024) 7188–7194.

[201] H.-M. Kwon, J.C. Bird, K.K. Varanasi, Increasing Leidenfrost point using micro-nano hierarchical surface structures, Appl. Phys. Lett. 103 (2013).

[202] C. Kruse, T. Anderson, C. Wilson, C. Zuhlke, D. Alexander, G. Gogos, S. Ndao, Extraordinary shifts of the leidenfrost temperature from multiscale micro/nanostructured surfaces, Langmuir 29 (2013) 9798–9806.

[203] P. Foltyn, D. Ribeiro, A. Silva, G. Lamanna, B. Weigand, Influence of wetting behavior on the morphology of droplet impacts onto dry-patterned micro-structured surfaces, Phys. Fluids 34 (2022).

[204] C.E. Clavijo, J. Crockett, D. Maynes, Hydrodynamics of droplet impingement on hot surfaces of varying wettability, Int. J. Heat Mass Tran. 108 (2017) 1714–1726.

[205] C.-T. Huang, C.-W. Lo, M.-C. Lu, Reducing contact time of droplets impacting superheated hydrophobic surfaces, Small 18 (2022) 2106704.

[206] V. Bertola, An impact regime map for water drops impacting on heated surfaces, Int. J. Heat Mass Tran. 85 (2015) 430–437.

[207] W. Zhang, T. Yu, J. Fan, W. Sun, Z. Cao, Droplet impact behavior on heated micro-patterned surfaces, J. Appl. Phys. 119 (2016).

[208] J.G. Leidenfrost, On the fixation of water in diverse fire, Int. J. Heat Mass Tran. 9 (1966) 1153–1166.

[209] A.-B. Wang, C.-H. Lin, C.-C. Chen, The critical temperature of dry impact for tiny droplet impinging on a heated surface, Phys. Fluids 12 (2000) 1622–1625.

[210] Y. Wakata, N. Zhu, X. Chen, S. Lyu, D. Lohse, X. Chao, C. Sun, How roughness and thermal properties of a solid substrate determine the Leidenfrost temperature: experiments and a model, Phys. Rev. Fluids 8 (2023) L061601.

[211] D. Prasad, A. Sharma, S. Dash, Influence of the substrate permeability on Leidenfrost temperature, Int. J. Heat Mass Tran. 178 (2021) 121629.

[212] N. Saneie, V. Kulkarni, K. Fezzaa, N.A. Patankar, S. Anand, Boiling transitions during droplet contact on superheated nano/micro-structured surfaces, ACS Appl. Mater. Interfaces 14 (2022) 15774–15783.

[213] N. Farokhnia, S.M. Sajadi, P. Irajizad, H. Ghasemi, Decoupled hierarchical structures for suppression of Leidenfrost phenomenon, Langmuir 33 (2017) 2541–2550.

[214] C.M. Weickgenannt, Y. Zhang, S. Sinha-Ray, I.V. Roisman, T. Gambaryan-Roisman, C. Tropea, A.L.J.P.r.E. Yarin, Statistical, nonlinear,, s.m. physics, Inverse-Leidenfrost phenomenon on nanofiber mats on hot surfaces, Phys. Rev. E 84 (3 Pt 2) (2011) 036310.

[215] N.R. Geraldi, G. McHale, B.B. Xu, G.G. Wells, L.E. Dodd, D. Wood, M.I. Newton, Leidenfrost transition temperature for stainless steel meshes, Mater. Lett. 176 (2016) 205–208.

[216] S.M. Sajadi, P. Irajizad, V. Kashyap, N. Farokhnia, H. Ghasemi, Surfaces for high heat dissipation with no Leidenfrost limit, Appl. Phys. Lett. 111 (2017).

[217] M. Wei, Y. Song, Y. Zhu, D.J. Preston, C.S. Tan, E.N. Wang, Heat transfer suppression by suspended droplets on microstructured surfaces, Appl. Phys. Lett. 116 (2020).

[218] J.D. Bernardin, C.J. Stebbins, I. Mudawar, Effects of surface roughness on water droplet impact history and heat transfer regimes, Int. J. Heat Mass Tran. 40 (1996) 73–88.

[219] W. Huang, L. Zhao, X. He, Y. Li, C.P. Collier, Z. Zheng, J. Liu, D.P. Briggs, J. Cheng, Low-temperature Leidenfrost-like jumping of sessile droplets on microstructured surfaces, Nat. Phys. (2024).

[220] L. Zhong, Z.J.N. Guo, Effect of surface topography and wettability on the Leidenfrost effect, Nanoscale 9 (19) (2017) 6219–6236.

[221] Y. Liu, L. Moevius, X. Xu, T. Qian, J.M. Yeomans, Z. Wang, Pancake bouncing on superhydrophobic surfaces, Nat. Phys. 10 (2014) 515–519.

[222] B. Zhang, C. Ma, H. Zhao, Y. Zhao, P. Hao, X.-Q. Feng, C. Lv, Effect of wettability on the impact force of water drops falling on flat solid surfaces, Phys. Fluids 35 (2023) 112111.

[223] G. Lagubeau, M. Le Merrer, C. Clanet, D. Quéré, Leidenfrost on a ratchet, Nat. Phys. 7 (2011) 395–398.

[224] Á.G. Marín, D. Arnaldo del Cerro, G.R.B.E. Römer, B. Pathiraj, A. Huis in 't Veld, D. Lohse, Capillary droplets on Leidenfrost micro-ratchets, Phys. Fluids 24 (2012).

[225] P. Bourrianne, C. Lv, D. Quéré, The cold Leidenfrost regime, Sci. Adv. 5 (2019) eaaw0304.

[226] A.B.D. Cassie, S. Baxter, Wettability of porous surfaces, Trans. Faraday Soc. 40 (1944) 546–551.

[227] D. Quéré, Wetting and roughness, Annu. Rev. Mater. Res. 38 (2008) 71–99.

[228] H. Chen, X. Li, D. Li, Superhydrophilic–superhydrophobic patterned surfaces: from simplified fabrication to emerging applications, Nanotech. Precis. Eng. 5 (2022) 035002.

[229] S. Park, J. Kim, C.H. Park, Superhydrophobic textiles: review of theoretical definitions, fabrication and functional evaluation, J. Eng. Fiber. Fabr. 10 (2015) 155892501501000401.

[230] U. Mehmood, F.A. Al-Sulaiman, B.S. Yilbas, B. Salhi, S.H.A. Ahmed, M.K. Hossain, Superhydrophobic surfaces with antireflection properties for solar applications: a critical review, Sol. Energ. Mat. Sol. c. 157 (2016) 604–623.

[231] Y. Rahmawan, L. Xu, S. Yang, Self-assembly of nanostructures towards transparent, superhydrophobic surfaces, J. Mater. Chem. A 1 (2013) 2955–2969.

[232] P. Dimitrakellis, E. Gogolides, Hydrophobic and superhydrophobic surfaces fabricated using atmospheric pressure cold plasma technology: a review, Adv. Colloid Interfac. 254 (2018) 1–21.

[233] A.A. Farag, E.A. Mohamed, A. Toghan, The new trends in corrosion control using superhydrophobic surfaces: a review, Corros. Rev. 41 (2023) 21–37.

[234] E. Kobina Sam, D. Kobina Sam, X. Lv, B. Liu, X. Xiao, S. Gong, W. Yu, J. Chen, J. Liu, Recent development in the fabrication of self-healing superhydrophobic surfaces, Chem. Eng. J. 373 (2019) 531–546.

[235] A. Krishnan, A.V. Krishnan, A. Ajith, S.M.A. Shibli, Influence of materials and fabrication strategies in tailoring the anticorrosive property of superhydrophobic coatings, Surf. Interfaces 25 (2021) 101238.

[236] N. Kaushal, A.K. Singh, Advancement in utilization of bio-based materials including cellulose, lignin, chitosan for bio-inspired surface coatings with special wetting behavior: a review on fabrication and applications, Int. J. Biol. Macromol. 246 (2023) 125709.

[237] D. Wang, Q. Sun, M.J. Hokkanen, C. Zhang, F.-Y. Lin, Q. Liu, S.-P. Zhu, T. Zhou, Q. Chang, B. He, Q. Zhou, L. Chen, Z. Wang, R.H.A. Ras, X. Deng, Design of robust superhydrophobic surfaces, Nature 582 (2020) 55–59.

[238] T.M. Thomas, I.U. Chowdhury, K. Dhivyaraja, P.S. Mahapatra, A. Pattamatta, M. K. Tiwari, Droplet dynamics on a wettability patterned surface during spray impact, Processes 9 (2021) 555.

[239] S. Singh, R. Kukreja, Experimental investigations on heat transfer enhancement of enhanced surfaces in spray cooling using HFE-649, Int. J. Multiphas. Flow 161 (2023) 104387.

[240] R. Xu, G. Wang, P. Jiang, Spray cooling on enhanced surfaces: a review of the progress and mechanisms, J. Electron. Packag. 144 (2021).

[241] J. Han, S. Shin, S. Oh, H.J. Hwang, D. Choi, C. Lee, Y. Nam, High-powered superhydrophobic pyroelectric generator via droplet impact, Nano Energy 126 (2024) 109682.

[242] J. Zhang, H. Wei, Y. Jin, B. Li, W. Niu, J. Zang, W. Lu, L. Chen, Impingement of ferrofluid droplets on superamphiphobic surfaces under magnetic fields, Phys. Fluids 35 (2023).

[243] N. Sahoo, G. Khurana, D. Samanta, P. Dhar, Collisional ferrohydrodynamics of magnetic fluid droplets on superhydrophobic surfaces, Phys. Fluids 33 (2021) 012012.

[244] N. Sahoo, P. Dhar, D. Samanta, Vertical magnetic field aided droplet-impact-magnetohydrodynamics of ferrofluids, Colloid. Surfaces a. 633 (2022) 127872.

[245] P. Shah, M.M. Driscoll, Drop impact dynamics of complex fluids: a review, Soft Matter 20 (2024) 4839–4858.

[246] Y.T. Aksoy, Y. Zhu, P. Eneren, E. Koos, M.R. Vetrano, The impact of nanofluids on droplet/spray cooling of a heated surface: a critical review, Energies 14 (2021) 80.

[247] P. Dhar, S.R. Mishra, D. Samanta, Onset of rebound suppression in non-Newtonian droplets post-impact on superhydrophobic surfaces, Phys. Rev. Fluids 4 (2019) 103303.

[248] K. Kamaluddin, G.C. Pal, P. Dhar, C.S. Sharma, D. Samanta, Parallel governing criteria for non-Newtonian droplet rebound suppression on superhydrophobic surfaces, Colloid. Surfaces a. 684 (2024) 133128.

[249] J.T. Pham, M. Paven, S. Wooh, T. Kajiya, H.-J. Butt, D. Vollmer, Spontaneous jumping, bouncing and trampolining of hydrogel drops on a heated plate, Nat. Commun. 8 (2017) 905.

[250] F. Zhang, X. Li, H. Li, J. Tang, G. Chen, L. Zhang, G. Li, Dynamic study of [Emim]Ac ionic liquid droplet impact on mildly heated solid surfaces, Int. Commun. Heat Mass 130 (2022) 105783.

[251] X.-D. Zhang, G. Yang, B.-Y. Cao, Bonding-enhanced interfacial thermal transport: mechanisms, materials, and applications, Adv. Mater. Interfaces 9 (2022) 2200078.

[252] J. Du, X. Wang, Y. Li, Q. Min, How an oxide layer influences the impact dynamics of galinstan droplets on a superhydrophobic surface, Langmuir 38 (2022) 5645–5655.

[253] G.V.V.S.V. Prasad, P. Dhar, D. Samanta, Postponement of dynamic Leidenfrost phenomenon during droplet impact of surfactant solutions, Int. J. Heat Mass Tran. 189 (2022) 122675.

[254] G.V.V.S. Vara Prasad, H. Sharma, N. Nirmalkar, P. Dhar, D. Samanta, Augmenting the Leidenfrost temperature of droplets via nanobubble dispersion, Langmuir 38 (2022) 15925–15936.

[255] G.V.V.S. Vara Prasad, M. Yadav, P. Dhar, D. Samanta, Morphed inception of dynamic Leidenfrost regime in colloidal dispersion droplets, Phys. Fluids 35 (2023) 012107.

[256] H. Li, S. Mei, L. Wang, Y. Gao, J. Liu, Splashing phenomena of room temperature liquid metal droplet striking on the pool of the same liquid under ambient air environment, Int. J. Heat Fluid Fl. 47 (2014) 1–8.

[257] X. Zhao, M. Qiao, Y. Zhou, J. Liu, Liquid metal droplet dynamics, Droplet 3 (2024) e104.

[258] Z. Zhou, F. Yan, G. Zhang, D. Wu, H. Xu, A study on the dynamic collision behaviors of a hydrous ethanol droplet on a heated surface, Processes 11 (2023) 1804.

[259] X. Tian, T. Verho, R.H.A. Ras, Moving superhydrophobic surfaces toward real-world applications, Science 352 (2016) 142–143.

[260] A.R. Jacob, D.P. Parekh, M.D. Dickey, L.C. Hsiao, Interfacial rheology of gallium-based liquid metals, Langmuir 35 (2019) 11774–11783.

[261] G. Pottker, A. Van Wassen, D.R. Brandt, A new Low-GWP dielectric fluid for two-phase immersion cooling, ASME 2023 International Technical Conference and Exhibition on Packaging and Integration of Electronic and Photonic Microsystems. San Diego, California, USA. October 24–26, 2023. V001T01A005. ASME.